Pharmacological Research 233 (2026) 109653

Contents lists available at ScienceDirect

Pharmacological Research

journal homepage: www.elsevier.com/locate/yphrs

Nε-(Carboxymethyl)lysine induces mitochondrial stress, inflammatory activation, and fibrogenic remodelling in multicellular human liver organoids

Jin Young Min [a,1], Min Ji Gu [b,1], Hye Min Kim [a,c,1], Donghwan Kim [b], Geul Bang [a], Sang-Yeop Lee [a,c], Hae Won Jung [a,c], Kwan Soo Hong [a,d], Dae Won Jun [e], Seung Min Lee [f], Sang Keun Ha [b,c,*], Eun Hee Han [a,c,**]

[a] Ochang Institute of Biological and Environmental Science, Korea Basic Science Institute (KBSI), Cheongju, 28119, Republic of Korea
[b] Food Functionality Research Division, Korea Food Research Institute, Jeollabuk-do, 55365, Republic of Korea
[c] University of Science and Technology (UST), Daejeon, 34113, Republic of Korea
[d] Department of Chemistry, Chung-Ang University, Seoul, 06974, Republic of Korea
[e] Department of Gastroenterology, Hanyang University College of Medicine, Seoul, 04763, Republic of Korea
[f] Department of Translational Medicine, Graduate School of Biomedical Science & Engineering, Hanyang University, Seoul, 04763, Republic of Korea

ARTICLE INFO

Keywords:
Nε-(carboxymethyl)lysine
Metabolic dysfunction-associated steatotic liver disease
Human liver organoids
AGE–RAGE signalling
Mitochondrial stress
Fibrogenic remodelling

ABSTRACT

Advanced glycation end-products (AGEs) accumulate in metabolic dysfunction-associated steatotic liver disease (MASLD); however, the contribution of individual AGE species remains poorly defined. We focused on Nε-(carboxymethyl)lysine (CML), a well-characterised AGE generated through glycoxidation and lipid peroxidation, and investigated its association with steatotic liver disease and its effects in multicellular liver models. AGE–RAGE pathway activity was analysed in public liver transcriptomic cohorts, and total AGEs and CML were quantified in human liver and serum. Free CML was then used as a defined experimental stimulus in mice, HepG2 2D/3D, and human induced pluripotent stem cell-derived liver organoid (HLO) models. AGE–RAGE pathway activity was associated with steatohepatitis-related features, whereas hepatic CML was selectively elevated in steatotic liver. Oral CML induced AGE–RAGE- and transforming growth factor beta-associated transcriptional changes in mice but minimal histological fibrosis, whereas HepG2 models showed limited CML-associated lipid accumulation. In contrast, HLOs exhibited concentration-dependent lipid accumulation and fibrogenic remodelling. Single-cell and functional analyses further revealed coordinated mitochondrial stress, inflammatory activation, stellate-cell remodelling, and collagen deposition. Selected responses were attenuated by pathway-targeted interventions, and patient serum cytokine and liver proteomic profiles showed partial concordance with HLO-associated signatures. Together, these findings identify hepatic CML as an AGE-related feature of steatotic liver disease and demonstrate coordinated mitochondrial, inflammatory, and fibrogenic responses to CML in multicellular HLOs. These results support the utility of HLOs for investigating AGE-specific mechanisms in human liver pathology.

1. Introduction

Advanced glycation end-products (AGEs) comprise a chemically heterogeneous group of adducts formed through non-enzymatic reactions involving reducing sugars, reactive carbonyl intermediates, and biomolecules. Because individual AGE species differ in their chemical origin, molecular form, tissue distribution, receptor interactions, and biological activity, treating AGEs as a single entity may obscure species-specific pathogenic effects. AGE–RAGE signalling has been implicated in oxidative stress, inflammation, and tissue remodelling across metabolic disorders, including chronic liver disease [1,2].

Among individual AGE species, Nε-(carboxymethyl)lysine (CML) is

* Corresponding author at: Food Functionality Research Division, Korea Food Research Institute, Jeollabuk-do, 55365, Republic of Korea.
** Corresponding author at: Ochang Institute of Biological and Environmental Science, Korea Basic Science Institute (KBSI), Cheongju, 28119, Republic of Korea.
E-mail addresses: skha@kfri.re.kr (S.K. Ha), heh4285@kbsi.re.kr (E.H. Han).
[1] These authors contributed equally to this work

https://doi.org/10.1016/j.phrs.2026.109653
Received 4 August 2026; Received in revised form 11 September 2026; Accepted 26 September 2026
Available online 28 September 2026
1043-6618/© 2026 The Authors. Published by Elsevier Ltd. This is an open access article under the CC BY-NC license (http://creativecommons.org/licenses/by-nc/4.0/).

particularly relevant to metabolic liver disease. In vivo, CML is commonly present as a lysine adduct on tissue proteins, whereas free CML can arise through protein turnover and may also be encountered through exogenous exposure [3,4]. These molecular forms are not necessarily biologically equivalent and may differ in tissue handling, receptor engagement, and downstream effects.

CML provides a rational focus for three reasons. First, it is one of the most abundant and extensively characterized AGE adducts detected in tissue proteins [3]. Second, CML can be generated through both glycoxidation and lipid peroxidation, linking its formation to the combined carbohydrate- and lipid-derived oxidative stress characteristic of metabolic dysfunction [5]. Third, CML-containing modified proteins have been reported to engage the receptor for advanced glycation end-products (RAGE), activate nuclear factor kappa B (NF-κB)-associated signalling, and alter inflammatory gene expression [6]. These properties distinguish CML from aggregate AGE measurements and support its investigation as a potential mediator at the interface of dysglycaemia, lipid overload, oxidative stress, and inflammatory signalling in metabolic dysfunction-associated steatotic liver disease (MASLD).

Clinical and experimental observations further support the hepatic relevance of CML. Increased endogenous CML formation has been reported in human fatty liver and has been associated with inflammatory signalling in experimental models of hepatic steatosis [7]. Increased levels of CML-modified AGEs have also been reported in chronic liver disease and cirrhosis [8]. In animal studies, long-term exposure to free CML altered metabolic parameters under high-fat dietary conditions, dietary CML aggravated hepatic steatosis, and CML–RAGE signalling was implicated in fatty liver progression [9–11]. These observations are consistent with a broader literature implicating AGEs in hepatic injury and fibrosis [12,13].

CML-associated fibrogenic effects have also been demonstrated in hepatic stellate-cell models. CML exposure increased oxidative stress and fibrogenic responses in hepatic stellate cells, whereas antioxidant interventions attenuated these effects [14,15]. More broadly, AGEs have been shown to promote hepatic stellate-cell proliferation and activation, induce NADPH oxidase-dependent reactive oxygen species generation, and exacerbate experimental hepatic fibrosis [13,16,17]. Collectively, these findings establish the biological plausibility of CML-associated stress in liver injury but do not clarify how metabolic, inflammatory, and stellate-cell responses are coordinated within a multicellular human liver context.

Important additional questions therefore remain. It is unclear whether local hepatic CML burden is adequately reflected by circulating CML or by aggregate AGE measurements. Clinical studies have demonstrated measurable circulating CML and other AGE species, but serum concentrations do not necessarily provide a direct measure of tissue AGE accumulation [18,19]. Furthermore, experimental responses may depend strongly on the model employed. Mouse models reproduce selected features of human steatotic liver disease but show limited transcriptomic concordance with human disease [20], while hepatoma-derived HepG2 systems have well-recognized limitations in differentiated hepatic function and metabolism [21].

Human liver spheroids and organoid systems offer complementary approaches for addressing these limitations. Primary human hepatocyte spheroids maintain key hepatic functions and have been used to model drug-induced liver injury and metabolic liver phenotypes [22]. Human hepatic 3D spheroids have also been established as models of steatosis and insulin resistance [23]. In parallel, human induced pluripotent stem cell-derived multicellular liver organoids (HLOs) incorporate hepatocyte-, macrophage/Kupffer-, and stellate-like populations within a shared three-dimensional microenvironment and reproduce features of steatosis, inflammation, and fibrogenic remodelling [24–26]. Because interpretation of multicellular injury responses depends on establishing both lineage composition and hepatic functional maturation before treatment, baseline characterization of the HLO model was incorporated into the present study. Importantly, single-cell analyses have demonstrated that HLO responses are stimulus dependent: oleic acid, palmitic acid, and transforming growth factor-β1 induce distinct inflammatory and fibrogenic states rather than a uniform injury phenotype [27]. Hess et al. specifically showed stimulus-dependent differences among OA-, palmitate-, and transforming growth factor beta 1 (TGF-β1)-treated organoid models, supporting this interpretation.

We therefore hypothesized that CML induces a distinct multicellular hepatic response characterized by mitochondrial stress in hepatocyte-like cells, inflammatory activation, and stellate-cell-associated fibrogenic remodelling. To experimentally isolate CML-specific effects from those of chemically heterogeneous AGE mixtures, we used free CML as a defined experimental stimulus in mechanistic studies, whereas measurements of tissue and serum CML were used to assess the corresponding human disease context. This distinction is important because experimental free-CML exposure should not be assumed to reproduce all biochemical forms or concentrations of tissue-associated CML in vivo.

To test this hypothesis, we first assessed AGE–RAGE pathway activity in public liver transcriptomic cohorts and quantified total AGEs and CML in human liver and serum. We then compared CML-associated responses across mouse, HepG2 2D/3D, and multicellular HLO systems. Bulk and single-cell transcriptomics, mitochondrial respiration assays, cytokine profiling, and pathway-targeted interventions were subsequently integrated to examine coordinated mitochondrial, immune-associated, and fibrogenic responses. Patient serum cytokine profiles and liver proteomic data were additionally analysed to evaluate translational concordance.

Accordingly, the present study makes three principal contributions. First, it distinguishes hepatic CML from aggregate AGE burden and circulating CML in the context of steatotic liver disease. Second, it defines the model dependence of CML-associated metabolic, inflammatory, and fibrogenic phenotypes across conventional and multicellular experimental systems. Third, it identifies coordinated mitochondrial, immune-associated, and fibrogenic responses to CML in a multicellular human liver model and evaluates whether selected components of these responses can be modulated by pathway-targeted interventions.

2. Methods

2.1. Animals

Five-week-old male C57BL/6 J mice were purchased from OrientBio, Inc. (Gwangju, Republic of Korea) and housed under controlled conditions (23 ± 1 °C, 55 ± 5% relative humidity, 12-h light/dark cycle), with food and water available ad libitum. Mice in the oral-exposure experiment were randomly assigned using a computer-generated sequence to vehicle-control, CML 10 mg/kg, or CML 20 mg/kg groups (n = 8 animals per group). CML (>95.0% purity; HeBei Sundia Meditech, Shijiazhuang, China) or distilled-water vehicle was administered orally once daily, 5 days per week, for 12 weeks. A high-fat-diet (HFD) group was included as a metabolic comparator in the indicated tissue analyses. At the study endpoint, animals were euthanized by isoflurane overdose and liver tissue and serum were collected. Eight mice were initially assigned to each experimental group; the number included in individual downstream analyses varied by assay and is specified in the corresponding figure legends. Detailed protocols for haematoxylin and eosin (H&E) staining, immunohistochemistry, RNA sequencing analysis, and RNA scope assays are provided in the Supplementary Methods.

2.2. Generation, maturation, and experimental use of human liver organoids

Human liver organoids (HLOs) were generated using a stepwise differentiation protocol adapted from Ouchi et al. [24]. Human induced pluripotent stem cells (hiPSCs; ChiPSC18, Y00305; Takara Bio, Shiga, Japan) at passages 3–5 were maintained under feeder-free conditions on

Matrigel-coated plates in mTeSR1 medium, with daily medium replacement. Differentiation was initiated on day 0. Definitive endoderm was induced during days 1–3 using activin A, BMP4, and sequential foetal calf serum supplementation. From days 4–6, foregut endoderm was induced in Advanced DMEM/F12 supplemented with B27, N2, FGF4 (500 ng/mL), and CHIR99021 (3 μM), with daily medium replacement.

On day 7, foregut-derived cells were dissociated and embedded in Matrigel at 5×10^4 cells per 50 μL dome to initiate three-dimensional hepatic endoderm organoid (HEO) formation. The cells were cultured through day 13 in HEO medium containing bFGF (5 ng/mL), EGF (20 ng/mL), VEGF165 (10 ng/mL), CHIR99021 (3 μM), and A83–01 (0.5 μM), with daily medium replacement. On day 13, HEOs were dissociated into single cells or small fragments and re-embedded in Matrigel. HEOs at passage 3 or lower were used for subsequent HLO maturation. HEO stocks used throughout the study were generated from three independent hiPSC differentiation batches and cryopreserved. Individual HEO aliquots were thawed as required and independently matured for subsequent experiments.

For hepatic maturation, HEOs were cultured in HEO medium supplemented with retinoic acid (2 μM) during days 14–17. From days 18–27, the organoids were cultured in hepatocyte culture medium supplemented with SingleQuots (Lonza, cat. no. CC-4182), oncostatin M (20 ng/mL), HGF (10 ng/mL), and dexamethasone (0.1 μM). The maturation medium was replaced every other day. Day 27 was designated as the mature-stage experimental time point based on organoid morphology, hepatic and biliary marker expression, and albumin and apolipoprotein B secretion.

Organoids of comparable size were selected by visual inspection and distributed across experimental groups. CML treatment was initiated on day 28. Unless otherwise specified, HLOs were treated with 250 μM CML for 72 h. For routine quantitative assays, each experimental replicate corresponded to one independently treated well containing multiple organoids, and at least five wells were analysed per condition. Assay-specific experimental units, including single-organoid measurements, are described in the corresponding methods and figure legends.

2.3. Experimental Methods

Detailed protocols for histology, immunohistochemistry, RNAscope, bulk and single-cell RNA sequencing, quantitative reverse transcription polymerase chain reaction, immunofluorescence, lipid staining, triglyceride measurement, cytokine profiling, proteomics, Seahorse XF analysis, lactate dehydrogenase (LDH) release, retinoid storage, primary-cell assays, and inhibitor experiments are provided in the Supplementary Methods. The HepG2 human hepatocellular carcinoma cell line (RRID:CVCL_0027; catalog no. KCLB 88065) was obtained from the Korean Cell Line Bank (Seoul, Republic of Korea). Unless otherwise specified, the routine unit of experimental replication was an independently treated well containing multiple organoids; single-organoid assays are identified explicitly.

2.4. Statistical analysis

Data are presented as mean ± standard error of the mean, unless otherwise specified. Independent animals, human participants, or independently treated wells were used as the units of analysis, as appropriate. Technical duplicate spots or measurements were averaged and were not treated as independent biological replicates. Statistical analyses were performed in GraphPad Prism version 10.3.1 (GraphPad Software, San Diego, CA, USA). For prespecified two-group or pairwise experimental comparisons, normality was assessed by the Shapiro–Wilk test and an unpaired two-tailed Student's *t*-test was used unless otherwise specified. Public-cohort analyses used two-sided unpaired Welch's *t*-tests; Holm adjustment was applied within each multi-group clinical classification, whereas single two-group comparisons were unadjusted. The overall distribution of recovered single-cell annotations between conditions was compared using Pearson's chi-square test. A two-sided P value, or adjusted P value where stated, < 0.05 was considered statistically significant. Exact n values, assay-specific comparisons, and significance thresholds are provided in the figure legends and plots.

3. Results

3.1. AGE–RAGE pathway activity is associated with steatohepatitis-related features, and hepatic CML is elevated in steatotic liver

To define the disease context of AGE–RAGE signalling without attributing the pathway signature to a specific AGE species, we calculated single-sample gene set enrichment analysis (ssGSEA) scores in three independent public liver transcriptomic cohorts. Diagnostic terms used in the original datasets were retained when reporting cohort-specific groups.

In GSE126848, AGE–RAGE pathway scores were higher in the nonalcoholic fatty liver (NAFL) and nonalcoholic steatohepatitis (NASH) groups than in controls, whereas the obese group did not differ significantly from controls (Fig. 1A). In GSE48452, the score was higher in NASH than in controls but was not significantly altered in the healthy-obese or steatosis groups. The score was also higher in samples classified as definite NASH (NAFLD activity score [NAS], 5–8) than in those classified as not NASH (NAS, 0–2), and in samples with lobular inflammation than in those without inflammation (Fig. 1B). In GSE89632, AGE–RAGE pathway activity was higher in NASH than in simple steatosis and was also elevated in samples classified by definite NASH, lobular inflammation, and fibrosis severity (Fig. 1C). The absence of significant differences in several obese, steatosis, and borderline-NASH comparisons indicates that increased AGE–RAGE pathway activity was not uniformly observed across all intermediate disease categories.

We next quantified total AGEs and CML in human liver tissue and serum. Total AGE concentrations did not differ significantly between the normal and steatosis groups in either liver tissue or serum (Fig. 1D). In contrast, hepatic CML was significantly higher in steatotic than in normal liver tissue, whereas serum CML did not differ significantly between the groups (Fig. 1E). Thus, among the AGE-related biochemical parameters measured, hepatic CML was the only parameter that differed significantly between the normal and steatosis groups.

Together, these transcriptomic analyses associate increased AGE–RAGE pathway activity with steatohepatitis-related diagnostic and histological features, whereas the biospecimen analysis identifies selective elevation of CML within steatotic liver tissue. Importantly, these human data do not establish CML as the upstream driver of the AGE–RAGE pathway signature. We therefore next examined the hepatic response to defined CML exposure in experimental models.

3.2. Oral CML induces hepatic molecular responses without overt fibrosis, whereas HepG2 models show limited CML-induced lipid accumulation

C57BL/6 J mice were assigned to vehicle-control or CML-treatment groups (10 or 20 mg/kg; $n = 8$ per group) and treated for 12 weeks (Fig. 2A). For the CML quantification shown in Fig. 2B, liver and serum samples from six animals per group were analysed using enzyme-linked immunosorbent assay in the control, 10-mg/kg CML, and HFD comparator groups. Hepatic CML concentrations were significantly higher in the 10-mg/kg CML and HFD groups than in controls, whereas serum CML was increased in the 10-mg/kg CML group but was not significantly altered in the HFD group (Fig. 2B).

Representative immunohistochemical staining showed increased hepatic CML immunoreactivity following CML administration, whereas the corresponding H&E-stained sections showed only limited morphological alterations (Fig. 2C). Sirius Red staining did not reveal overt collagen deposition in the CML-treated groups under the tested

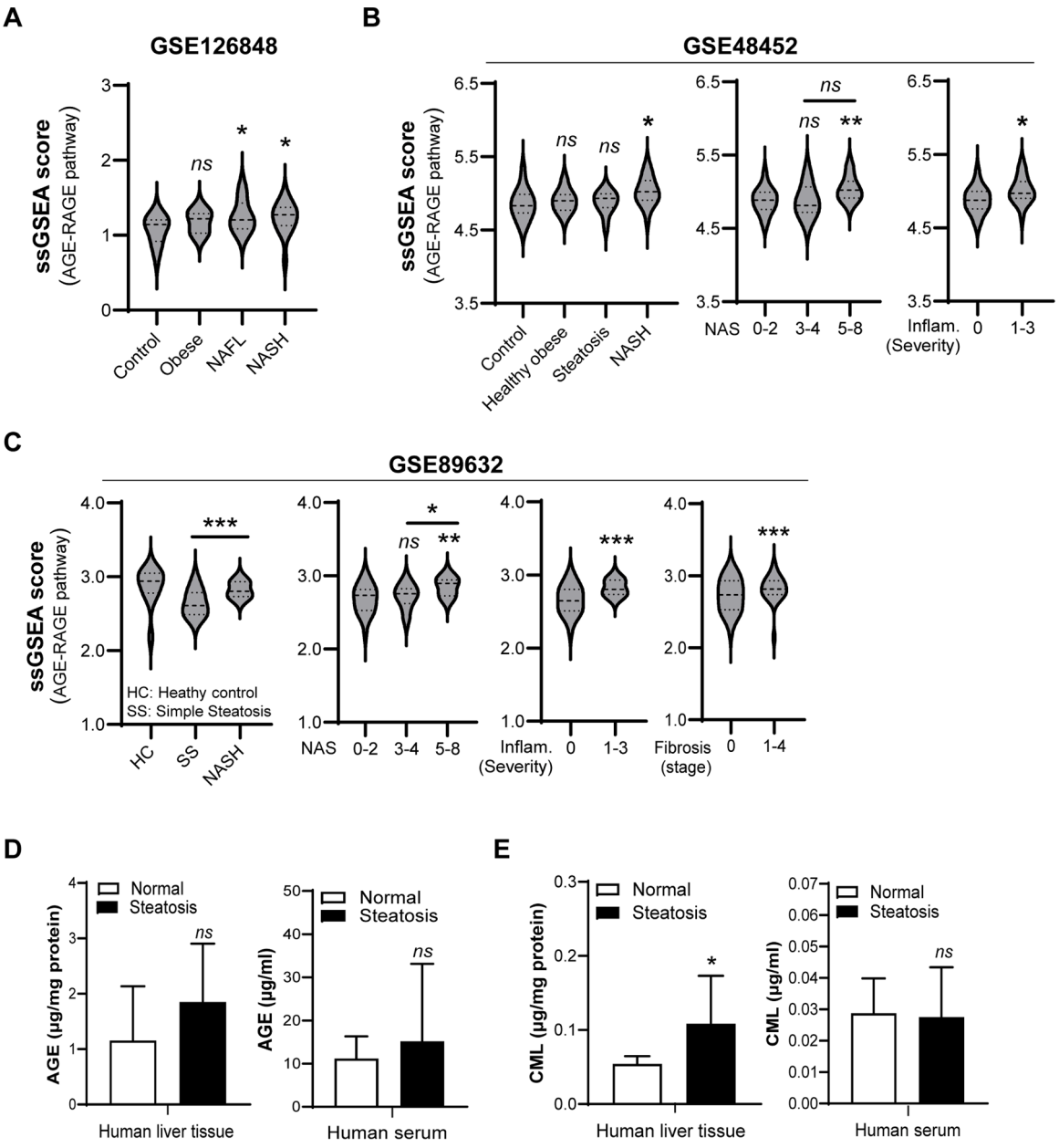

Fig. 1. AGE–RAGE pathway activity across steatosis- and NASH-related clinical features and CML accumulation in human liver. (A) AGE–RAGE pathway ssGSEA scores in the GSE126848 cohort according to diagnostic group (Control, Obese, NAFL, and NASH). (B) Scores in preoperative liver samples from the GSE48452 cohort according to diagnostic group, NAS, and lobular inflammation severity. Post-bariatric surgery samples were excluded. (C) Scores in the GSE89632 cohort according to diagnostic group, NAS, lobular inflammation severity, and fibrosis stage. (D) Total AGE concentrations in human liver tissue and serum from control and steatosis subjects. No significant between-group differences were observed. (E) CML concentrations in matched biospecimen types. Hepatic CML was increased in steatosis, whereas serum CML was unchanged. Violin plots show individual ssGSEA scores with medians and quartiles; ELISA data are presented as mean ± SEM. Pairwise comparisons were performed using two-sided unpaired Welch's *t*-tests, with Holm adjustment within each multi-group clinical classification. Reference groups were the first category shown in each plot. Symbols for two-group ELISA comparisons indicate unadjusted P values. *P < 0.05, **P < 0.01, and ***P < 0.001; ns, not significant. AGE, advanced glycation end-product; CML, Nε-(carboxymethyl)lysine; ELISA, enzyme-linked immunosorbent assay; HC, healthy control; NAS, NAFLD activity score; NAFL, nonalcoholic fatty liver; NASH, nonalcoholic steatohepatitis; SS, simple steatosis; ssGSEA, single-sample gene set enrichment analysis.

conditions, in contrast to the HFD comparator (Fig. 2D). These histological observations therefore support increased hepatic CML accumulation following oral exposure but do not indicate the development of established fibrosis during the treatment period.

To determine whether molecular responses were detectable despite the limited histological changes, we compared liver transcriptomes from control mice and mice receiving 20 mg/kg CML. At the applied thresholds (|log2 fold change| > 0.5 and $P < 0.05$), 494 genes were differentially expressed, including 255 upregulated and 239 downregulated genes (Fig. S1B). Unsupervised clustering separated the CML-treated and control transcriptional profiles (Fig. S1C), while pathway analysis identified AGE–RAGE signalling, TGF-β signalling, lipid and atherosclerosis, cell-adhesion, and related pathways among the enriched terms (Fig. S1D). RNAscope analysis independently demonstrated a dose-related increase in hepatic TGF-β RNA signals in the 10- and 20-mg/kg CML groups (Fig. S1E). Thus, oral CML elicited measurable hepatic molecular responses despite the absence of overt histological fibrosis under these experimental conditions.

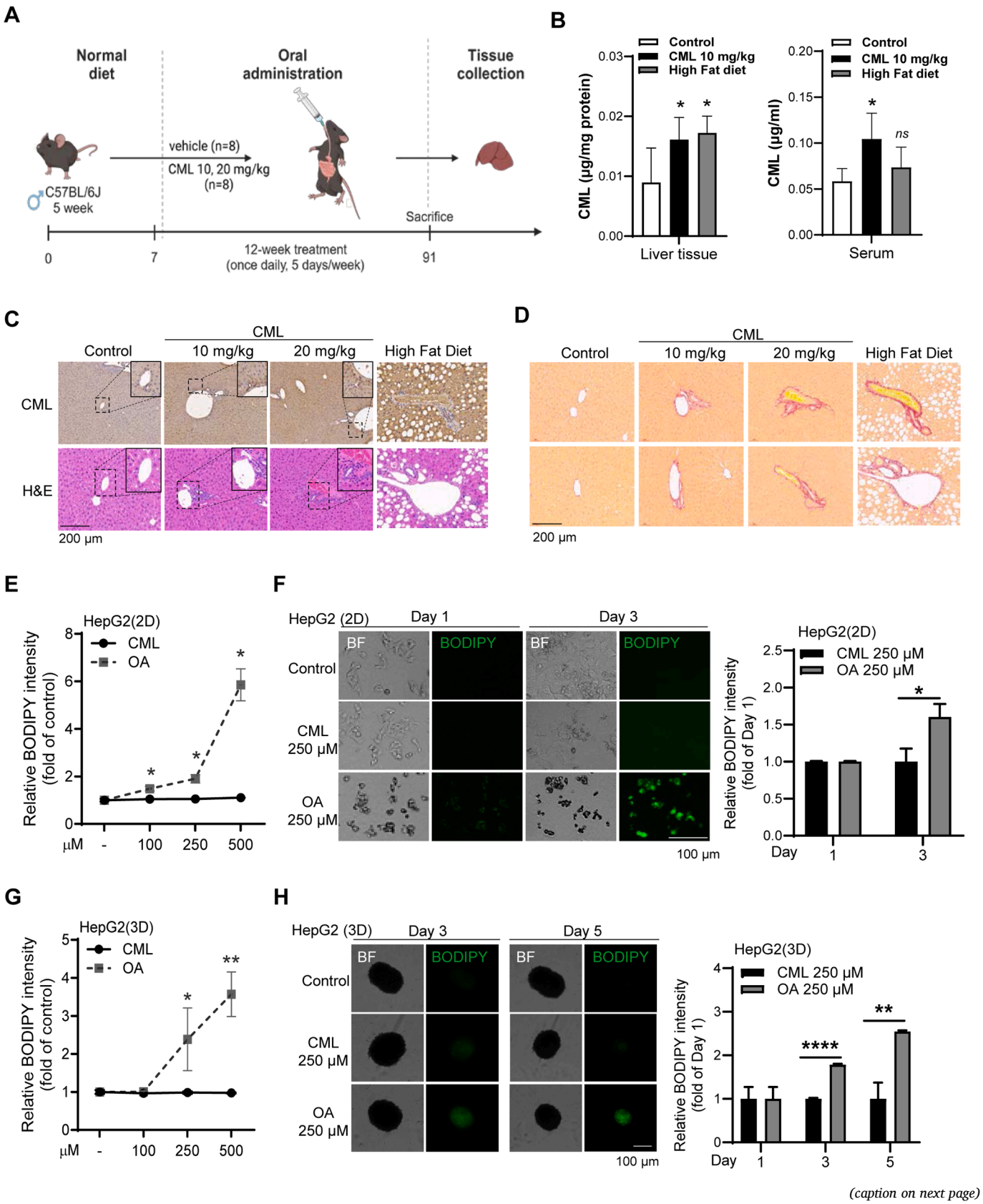

(caption on next page)

Fig. 2. Conventional in vivo and hepatoma-based models incompletely reproduce CML-associated hepatic responses. (A) Experimental design for oral CML administration in C57BL/6 J mice. The mice received vehicle or CML (10 or 20 mg/kg, once daily, 5 days/week) for 12 weeks, followed by liver tissue collection for downstream analyses. (B) CML levels in mouse liver tissue (left) and serum (right) measured by ELISA across groups (control, CML 10 mg/kg, and high-fat diet as indicated, n = 6). Data are shown as means ± SEMs; statistical significance is indicated on the plot. (C) Representative images of liver sections stained for CML (immunohistochemistry; top row) and H&E (bottom row) from control, CML-treated (10 and 20 mg/kg), and high-fat diet groups. Scale bar, 200 μm. (D) Representative Sirius Red staining images of liver sections from the indicated groups. Scale bar, 200 μm. HepG2 2D/3D models (OA vs. CML, matched conditions). (E) Concentration-dependent BODIPY fluorescence in HepG2 monolayers after 3 days of CML or OA treatment. (F) Representative bright-field (BF) and BODIPY images of HepG2 2D monolayers treated with OA (250 μM) or CML (250 μM) at days 1 and 3. Scale bar, 100 μm. Quantification of BODIPY fluorescence intensity in HepG2 2D cultures treated with OA (250 μM) or CML (250 μM), normalized to day 1 (fold of day 1), as indicated. (G) Concentration-dependent BODIPY fluorescence in HepG2 spheroids after 3 days of CML or OA treatment. (H) Representative BF and BODIPY images of HepG2 3D spheroids treated with OA (250 μM) or CML (250 μM) at days 3 and 5. Scale bar, 100 μm. Quantification of BODIPY fluorescence intensity in HepG2 3D spheroids treated with OA (250 μM) or CML (250 μM), normalized to day 1 (fold of day 1), as indicated. Data are presented as means ± SEMs. Statistical significance was determined using Student's t-test or ANOVA, where appropriate (*$P < 0.05$, **$P < 0.01$, ***$P < 0.001$, ****$P < 0.0001$). CML, Nε-carboxymethyl-lysine; H&E, haematoxylin and eosin; OA, oleic acid; BF, bright-field.

We next examined whether simplified hepatic cell systems reproduced the CML-associated phenotype. Primary mouse hepatocytes, hepatic stellate cells, and Kupffer cells maintained viability across the tested 0–3 μM CML range (Fig. S1A), indicating no detectable loss of viability under these specific exposure conditions. In HepG2 monolayers, CML at 100–500 μM produced little change in BODIPY fluorescence, whereas OA induced concentration- and time-associated lipid accumulation (Fig. 2E, F). A similar contrast was observed in HepG2 spheroids: OA increased BODIPY fluorescence on days 3 and 5, whereas CML-treated spheroids remained close to their baseline levels (Fig. 2G, H). Thus, under the conditions tested, HepG2 2D and 3D models readily reproduced the OA-associated lipid phenotype but showed only limited CML-induced lipid accumulation.

Together, these findings indicate that oral CML can induce hepatic molecular changes in mice without producing overt fibrosis during the tested treatment period, while HepG2-based models incompletely reproduce the CML-associated lipid phenotype. This model-dependent response provided the rationale for evaluating CML in a multicellular HLO system.

3.3. Characterization of the multicellular hepatic identity and function of HLOs

HLOs were generated from hiPSCs through sequential definitive endoderm, foregut, hepatic endoderm organoid, and hepatic maturation stages (Fig. 3A). The intermediate HEOs could be expanded, cryopreserved, and recovered while maintaining organoid morphology during subsequent culture (Fig. S2). During differentiation, the expression of lineage-associated genes, including CK19, AFP, ALB, HNF4A, HNF1B, and CDX2, changed progressively across hiPSCs, HEOs, HLOs, and adult liver tissue, consistent with hepatic specification and maturation (Fig. 3B).

Immunofluorescence staining further confirmed the expression and spatial organization of hepatic and epithelial markers in untreated HLOs, with additional comparative characterization provided in Fig. S3A and Fig. S3B. ALB and AAT expression supported hepatocyte-like differentiation, whereas CK19 and SOX9 indicated the presence of biliary-like cells. ZO-1 and F-actin staining demonstrated epithelial polarity and structural organization, while vimentin-positive cells indicated the presence of a mesenchymal cellular component (Fig. 3C).

Proteomic analysis further showed that HLOs expressed proteins associated with hepatocytes, cholangiocytes, stellate cells, and Kupffer cells, although their expression profiles remained distinct from those of adult liver tissue and HEOs (Fig. 3D). Consistently, cluster-level analysis of the untreated HLO scRNA-seq dataset showed lineage-associated expression patterns across the annotated cell populations. The hepatocyte-like cluster showed relatively higher expression of APOB, CPS1, and ASS1, whereas the cholangiocyte-like cluster showed higher expression of KRT19, EPCAM, and CLDN7. The stellate-like cluster showed preferential expression of the extracellular matrix-associated genes COL1A1 and COL3A1; LRAT was also detected but was not restricted to this cluster. The putative Kupffer-like cluster showed relatively higher expression of the macrophage/myeloid-associated genes LYZ, FCER1G, and APOE (Fig. 3E). Finally, HLOs showed significantly greater apolipoprotein B and albumin secretion than HEOs, together with increased CYP3A4 activity, demonstrating acquisition of hepatic secretory and metabolic functions during maturation (Fig. 3F). Additional CYP3A4 measurements comparing hiPSCs and HLOs at the indicated time points further supported maintenance of hepatic metabolic activity in the differentiated HLO model (Fig. S3C). Together, these orthogonal imaging, transcriptomic, proteomic, and functional measurements support the presence of multiple hepatic lineage-associated cellular components and hepatic secretory maturation in untreated HLOs before CML exposure. These findings support the use of day-27 HLOs as the mature-stage multicellular hepatic model for the subsequent CML experiments.

3.4. CML induces dose- and time-related lipid accumulation and a transcriptional state distinct from OA in HLOs

We first defined the concentration dependence of the HLO lipid response. After 3 days of exposure, CML increased BODIPY fluorescence in a dose-related manner beginning at 100 μM, with larger increases at 250 and 500 μM (Fig. 4A; Fig. S4A). In a separate 24-h membrane-injury assay, 250 μM CML did not significantly increase LDH release above control, whereas 500 μM CML caused a marked increase; OA at 250 μM also increased LDH release (Fig. 4B). Based on these findings, 250 μM was selected as the principal condition for subsequent mechanistic analyses because it produced a robust lipid-accumulation phenotype without a detectable increase in acute LDH release, whereas 500 μM was treated as a higher-concentration condition.

At 250 μM, CML-associated lipid accumulation increased progressively over time through day 15, whereas OA produced a larger late BODIPY response (Fig. 4C; Fig. S4B). Day-3 imaging confirmed increased BODIPY-positive lipid droplets in CML-treated HLOs (Fig. 4D), and Oil Red O staining provided an independent neutral-lipid readout (Fig. 4E). H&E-stained sections showed vacuolated and disorganized areas after both CML and OA exposure (Fig. 4F). AAT fluorescence was reduced under both conditions (Fig. 4G), and triglyceride content increased after CML exposure, although the increase induced by OA was substantially greater (Fig. 4H). SF44 staining and combined holotomographic/BODIPY imaging further supported intracellular lipid accumulation in CML-treated HLOs (Fig. S4D,E; Videos S1 and S2). Together, these complementary imaging, histological, and biochemical readouts establish a reproducible CML-associated lipid-accumulation phenotype in HLOs.

Supplementary material related to this article can be found online at doi:10.1016/j.phrs.2026.109653.

Under matched conditions, CEL, MG-H1, and MGO did not produce a BODIPY pattern as prominent as that observed with CML (Fig. S4C), indicating that the lipid phenotype was not uniformly reproduced by the other AGE-related compounds tested. In addition, an anti-RAGE antibody attenuated the CML-associated increase in BODIPY fluorescence (Fig. S4F), supporting the involvement of RAGE-associated signalling in

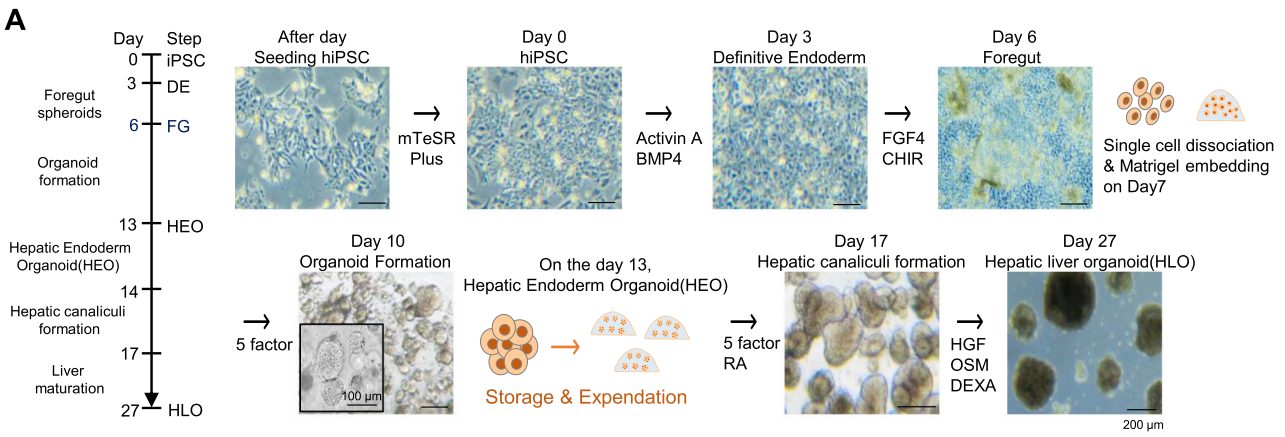

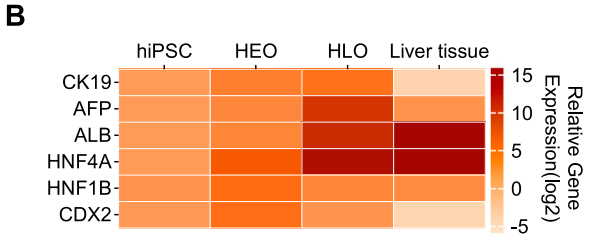

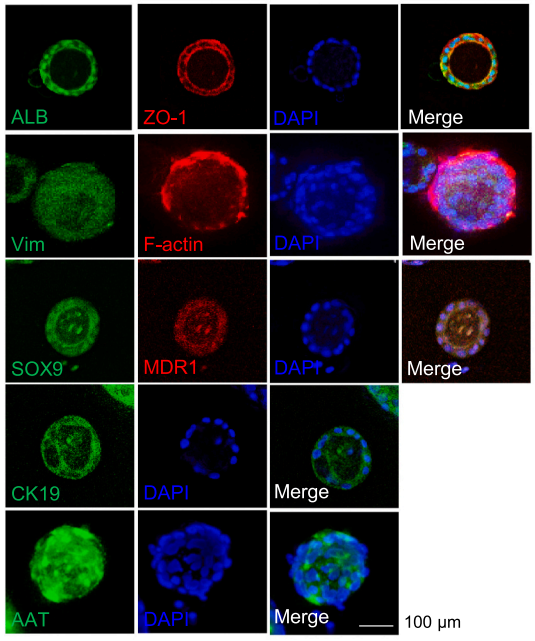

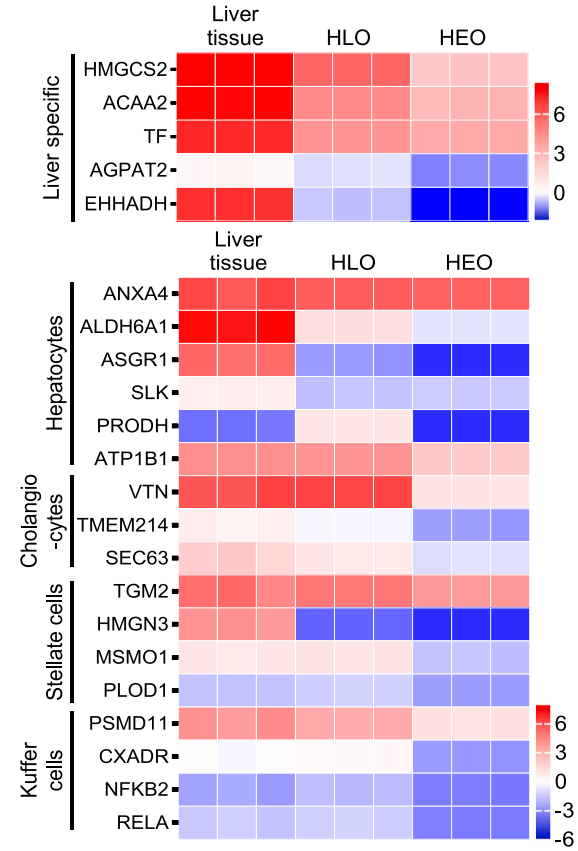

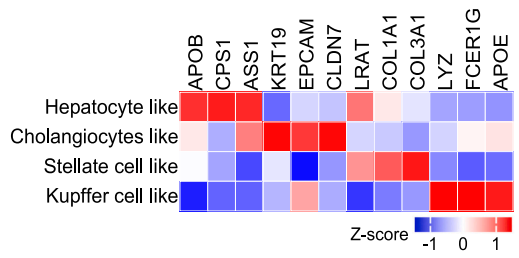

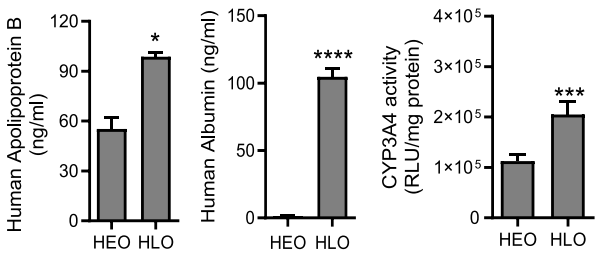

(caption on next page)

Fig. 3. Baseline characterization of multicellular identity and hepatic function in human liver organoids. (A) Differentiation schematic and representative bright-field images from hiPSCs through HEO and HLO stages. HEOs were cryopreserved and expanded before hepatic maturation. (B) qRT-PCR of CK19, AFP, ALB, HNF4A, HNF1B, and CDX2 in hiPSCs, HEOs, HLOs, and adult human liver RNA. (C) Representative immunofluorescence images of untreated HLOs stained for ALB and ZO-1, vimentin and F-actin, SOX9 and MDR1, CK19, and AAT, with DAPI counterstaining. Scale bar, 100 μm. (D) Relative abundance of selected hepatocyte-, cholangiocyte-, stellate-cell-, and Kupffer-cell-associated proteins in adult liver tissue, HLOs, and HEOs. (E) Heatmap of row-wise z-scores calculated from the average expression of selected lineage-associated genes across annotated hepatocyte-like, cholangiocyte-like, stellate-like, and Kupffer-like clusters in the untreated HLO scRNA-seq dataset. The displayed genes were APOB, CPS1, and ASS1 for the hepatocyte-like cluster; KRT19, EPCAM, and CLDN7 for the cholangiocyte-like cluster; LRAT, COL1A1, and COL3A1 for the stellate-like cluster; and LYZ, FCER1G, and APOE for the Kupffer-like cluster. Colors indicate relative row-scaled expression within each gene and should not be interpreted as absolute expression differences across genes. (F) Apolipoprotein B, albumin and CYP3A4 in HEO and HLO supernatants. Data are mean ± SEM; unpaired two-tailed Student's *t*-test, *P < 0.05 and ****P < 0.0001.

the lipid-accumulation response under the tested conditions. Because the readout was BODIPY fluorescence, this experiment evaluated lipid accumulation rather than intracellular CML uptake.

Although both CML and OA increased lipid-related readouts, bulk RNA sequencing separated control-, CML-, and OA-treated HLOs in the global expression heatmap and principal-component analysis (Fig. 4I). These findings indicate that CML and OA induce distinguishable global transcriptional states despite partially overlapping lipid phenotypes. The transcriptional separation does not by itself establish distinct causal mechanisms, but it supports the conclusion that the CML-associated HLO response is not simply equivalent to OA-induced lipotoxicity. This divergence provided the rationale for subsequent single-cell analyses aimed at identifying the cell populations and molecular programs associated with the CML response.

3.5. Single-cell profiling identifies shifts in recovered cell composition and candidate cell-type-associated programs after CML exposure

Single-cell RNA sequencing of dissociated control and CML-treated HLOs identified hepatocyte-like, Kupffer cell-like, stellate cell-like, and cholangiocyte-like clusters in both conditions (Fig. 5A; Fig. S5A–C). The control and CML-treated samples were processed separately without pooling, with at least 10,000 live cells used as input for each condition; 5698 control cells and 2102 CML-treated cells were recovered for analysis. The overall distribution of the four annotated cell populations differed significantly between conditions (Pearson's chi-square test, $P = 0.000058$). The hepatocyte-like fraction decreased from 63.0% in control HLOs to 34.0% after CML exposure, whereas the Kupffer cell-like fraction increased from 10.8% to 33.9% and the stellate cell-like fraction from 17.7% to 25.6%; the cholangiocyte-like fraction changed from 8.5% to 6.3% (Fig. 5A; Fig. S5A). These findings demonstrate a marked condition-associated shift in the composition of the recovered single-cell libraries. Because the analysis was based on dissociated-cell recovery, however, these differences cannot be interpreted directly as changes in true in-organoid cell abundance.

Within the hepatocyte-like cluster, differentially expressed genes were associated with mitochondrial inner membrane, electron transport, respirasome, ATP synthesis, response to hypoxia, and cellular respiration terms (Fig. 5B). The presence of both upregulated and downregulated genes within these categories indicates remodelling of mitochondrial-associated transcriptional programs rather than uniform suppression of mitochondrial function. In Kupffer cell-like cells, enriched terms included fatty-acid metabolism, long-chain fatty-acid transport, receptor binding, and cell-surface or cortical compartments (Fig. 5C), supporting altered lipid-handling and cell-interaction-associated programs after CML exposure.

In the global CML-versus-control comparison across recovered cells, 103 genes met the stated differential-expression thresholds, including 80 downregulated and 23 upregulated genes (Fig. 5D). Pathway enrichment identified IL-10 signalling, assembly of collagen fibrils and other multimeric structures, collagen degradation, insulin processing, and ion-channel-related pathways among the prominent terms (Fig. 5E). In addition, the inferred active-state fraction was higher among recovered stellate cell-like cells after CML exposure (Fig. 5F; Fig. S5D), consistent with a shift toward a more activated stellate-associated transcriptional state.

Together, these single-cell analyses reveal cell-type-associated changes encompassing mitochondrial, lipid-handling, inflammatory, and matrix-remodelling programs in CML-treated HLOs. These findings provided the rationale for subsequent functional experiments assessing mitochondrial bioenergetics, inflammatory mediators, and stellate-associated fibrogenic remodelling. The single-cell data alone, however, do not establish a temporal or directional hepatocyte-to-Kupffer-to-stellate signalling cascade.

3.6. Functional assays demonstrate context-dependent hepatocyte injury and concurrent bioenergetic, inflammatory, and fibrogenic responses

We first examined whether the response of isolated primary mouse hepatocytes to low-micromolar CML was influenced by a lipid-loaded context. After 24 h, CML alone produced little LDH release across the tested 0.01–5 μM range, whereas LDH release was greater at the upper end of the CML concentration range in the presence of 200 μM OA (Fig. 6A). MitoSOX fluorescence showed only limited changes across the tested conditions (Fig. 6B), whereas the JC-1 ratio was significantly increased at 5 μM CML under OA coexposure (Fig. 6C). Because an increased rather than decreased JC-1 ratio was observed, these data do not indicate mitochondrial depolarization. Collectively, these findings indicate that CML-associated injury and mitochondrial alterations were more evident in a lipid-loaded hepatocyte context than with CML alone.

We next directly assessed mitochondrial respiration in HLOs. After 2 h of exposure to 250 μM CML, the OCR profile was increased relative to control (Fig. 6D), with higher basal respiration, proton leak, ATP-linked respiration, maximal respiration, and spare respiratory capacity (Fig. S6A). A 100 μM CML condition produced smaller changes, whereas a 0.5-h exposure affected only selected parameters and did not reproduce the broader respiratory profile observed after 2 h (Fig. S6A,B). These findings demonstrate acute bioenergetic remodelling characterised by increased respiratory activity together with increased proton leak, consistent with mitochondrial stress rather than a generalized loss of respiration. In parallel, CML altered the expression of metabolic and hepatic genes, including increases in G6PC1, SLC2A1, and PCK1 and decreases in PDK4, FXR, EPCAM, BAAT, SLC27A5, SREBF1, and APOA4 (Fig. 6E; Fig. S6C). Together, these findings support coordinated mitochondrial and metabolic remodelling in CML-treated HLOs, although the transcriptional changes do not directly establish corresponding changes in enzyme activity or metabolic flux.

Secretome profiling was performed after 3 days of CML exposure using one cytokine-array membrane per condition. Each analyte was represented by duplicate capture-antibody spots, and reference-normalized signal intensities were used as a semiquantitative screen of CML-associated changes. The resulting profile showed altered signals among selected DAMP-, inflammation-, and fibrosis-associated mediators (Fig. 6F; Fig. S6D), and pathway analysis associated these changes with several signalling categories, including NF-κB and hepatic-fibrosis signalling (Fig. 6G; Fig. S6E). Independent assays further demonstrated increased TNF-α secretion and IL6 mRNA expression after CML exposure (Fig. 6H), providing orthogonal evidence of inflammatory activation at the whole-organoid level. Because the cytokine-array duplicate spots are technical replicates rather than independent

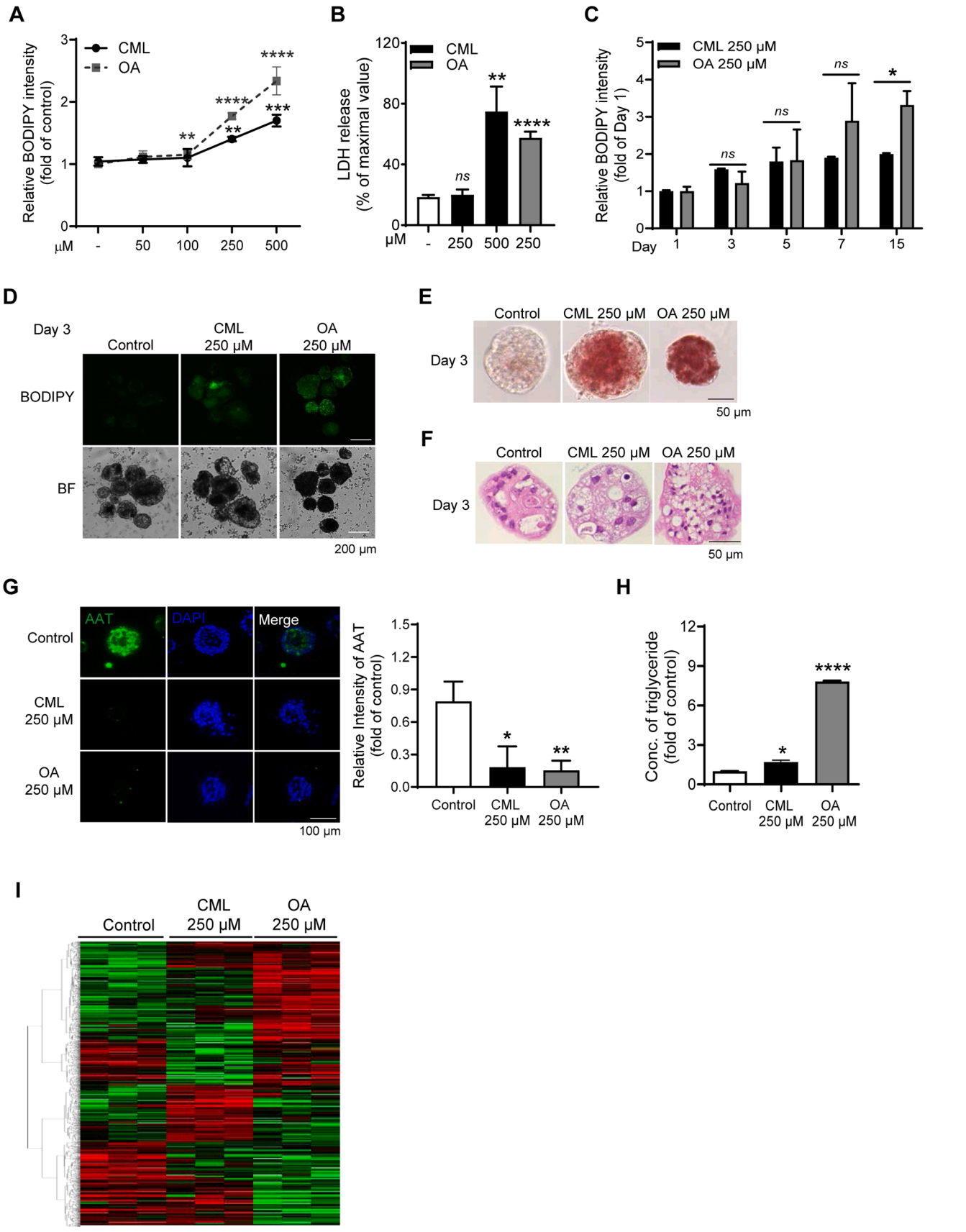

(caption on next page)

Fig. 4. Dose- and time-dependent CML-induced lipid accumulation and distinct transcriptional remodelling in human liver organoids. (A) BODIPY fluorescence after 3-day treatment with the indicated concentrations of CML or OA. (B) LDH release after 24-h treatment with CML (250 or 500 μM) or OA (250 μM), expressed relative to maximum release. (C) Time-course quantification of lipid accumulation in HLOs treated with OA (250 μM) or CML (250 μM), measured as relative BODIPY fluorescence intensity (fold of day 1) at the indicated time points (days 1–15). (D) Representative bright-field (BF) and BODIPY images of HLOs at day 3 under control, CML (250 μM), or OA (250 μM) conditions. Scale bar, 200 μm.(E) Oil Red O staining of neutral lipid droplets in HLOs at day 3 following treatment with control, CML (250 μM), or OA (250 μM). Scale bar, 50 μm. (F) H&E staining of HLO sections at day 3 showing tissue-level structural changes under CML or OA exposure (e.g., lipid vacuolation and cellular disorganization). Scale bar, 50 μm. (G) Immunofluorescence staining for α1-antitrypsin (AAT) in HLOs at day 3, with nuclei counterstained with DAPI. Scale bar, 100 μm. Quantification of AAT fluorescence intensity at day 3 (fold of control). (H) Intracellular triglycerides after CML (250 μM) or OA (250 μM) treatment. (I) Bulk RNA-seq heatmap showing distinct global transcriptional patterns among control-, CML-, and OA-treated HLOs, indicating stimulus-specific programs. Data are presented as means ± SEMs. Statistical significance was determined using Student's *t*-test or ANOVA, where appropriate (*P < 0.05, **P < 0.01, ***P < 0.001, ****P < 0.0001; ns, not significant). OA, oleic acid; CML, Nε-carboxymethyl-lysine; HLO, human liver organoid; BODIPY, 4,4-difluoro-1,3,5,7,8-pentamethyl-4-bora-3a,4a-diaza-s-indacene; H&E, haematoxylin and eosin; AAT, α1-antitrypsin.

biological samples, the array was interpreted as a semiquantitative screening analysis.

Fibrogenic remodelling was subsequently evaluated using independent molecular and phenotypic endpoints. CML increased COL1A1, ACTA2, LRP1, and PDGFRB transcript levels (Fig. 6I). Consistently, concentration-response analysis demonstrated concentration-related changes in COL1A1, ACTA2, LRP1, PDGFRB, IL6 and TNF-α expression, with the most prominent responses generally observed at 250 and 500 μM CML (Fig. S6F). In the retinoid-storage assay, HLOs were exposed to CML for 72 h, with all-trans-retinoid added during the final 24 h; CML significantly reduced retinoid fluorescence (Fig. 6J), consistent with loss of a quiescent stellate-associated phenotype. Masson's trichrome staining further demonstrated increased collagen-positive area after CML exposure, quantified using AIVIA relative to the total organoid tissue area (Fig. 6K). In matched comparisons, CML induced stronger changes in several stellate-activation-associated transcripts than CEL or MG-H1 under the tested conditions (Fig. S6G), supporting a comparatively stronger fibrogenic response to CML within this experimental panel.

Together, these orthogonal metabolic, inflammatory, molecular, and histological readouts demonstrate coordinated bioenergetic, inflammatory, and fibrogenic remodelling in CML-treated HLOs. The convergence of these independent assays supports the ability of the multicellular HLO system to capture multiple components of the CML-associated hepatic response. However, the experiments do not resolve the cellular source of each measured mediator or establish immune-cell-mediated stellate activation as a defined causal sequence.

Overall, CML induced concurrent lipid accumulation, mitochondrial and metabolic remodelling, inflammatory activation, and fibrogenic remodelling in multicellular HLOs. These findings provide a functional basis for the coordinated response identified by the transcriptomic analyses and support the utility of HLOs for investigating multicellular CML-associated liver pathology, while the temporal order and causal directionality of these responses remain to be defined.

3.7. *Patient biospecimens show partial concordance with inflammatory and tissue-remodelling signatures observed in CML-treated HLOs*

To assess whether response themes observed in CML-treated HLOs were also represented in human steatosis, we analysed serum cytokine profiles from 12 participants (normal, n = 6; steatosis, n = 6) and liver-tissue proteomes from six participants (normal, n = 3; steatosis, n = 3; Tables 1 and 2). For the displayed serum cytokine array, one representative specimen from each group was analysed, and duplicate capture spots for each analyte were normalized to the membrane reference spots. This semiquantitative comparison showed higher signals for several DAMP-, inflammation-, and fibrosis-associated mediators and lower signals for others in the displayed steatosis specimen (Fig. S7A–C).

In liver tissue, proteomic analysis identified 425 proteins with higher and 95 with lower abundance in steatosis at the applied thresholds (Fig. S7D). Enrichment analysis identified IL-6–JAK–STAT3 signalling, inflammatory response, apical-junction, and p53-related pathways among the prominent terms (Fig. S7E).

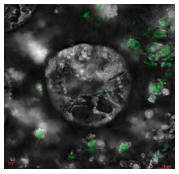

Video S2. Supplementary material related to this article can be found online.A video clip is available online. Supplementary material related to this article can be found online at doi:10.1016/j.phrs.2026.109653.

Together, these patient-derived data indicate that inflammatory and tissue-remodelling themes observed in CML-treated HLOs are also represented, at least in part, in human steatosis biospecimens, supporting the translational relevance of the HLO-associated response. However, because the serum cytokine array was a semiquantitative comparison of one representative specimen per group, and because no formal cross-dataset overlap analysis or individual-level association between hepatic CML burden and these signatures was performed, these findings are best interpreted as partial thematic concordance rather than clinical validation of a CML-driven mechanism.

3.8. *Pharmacological perturbations attenuate selected CML-associated phenotypes*

We used pharmacological perturbations to examine whether selected HLO phenotypes were sensitive to interventions targeting oxidative stress, glucose-dependent metabolism, macrophage-associated activity, and NF-κB-related signalling. For the lipid, LDH, and retinoid endpoints, HLOs were co-treated with 250 μM CML and the indicated compounds for 72 h. Co-treatment with N-acetylcysteine (NAC), clodronate, or 2-deoxy-D-glucose (2DG) significantly reduced CML-associated BODIPY fluorescence (Fig. 7A; Fig. S8A), indicating that the CML-associated lipid phenotype is sensitive to pharmacological modulation of oxidative, metabolic, and macrophage-associated processes. Comparative imaging of hiPSCs, HepaRG cells, and HLOs further supported the applicability of the retinoid-associated readout to the differentiated hepatic model (Fig. S8B).

In a separate 72-h inhibitor experiment, 250 μM CML increased LDH release relative to the concurrent control, whereas NAC and 2DG significantly reduced LDH release relative to CML alone (Fig. 7B). This finding differed from the 24-h LDH assay shown in Fig. 4B, in which 250 μM CML did not significantly increase LDH release. The difference may reflect the longer exposure period and distinct experimental context, suggesting that membrane injury becomes more evident with prolonged CML exposure. These results further indicate that oxidative and metabolic processes contribute to CML-associated cellular injury under prolonged exposure conditions.

CML reduced retinoid fluorescence, whereas co-treatment with NAC, clodronate, or 2DG significantly increased the signal relative to CML

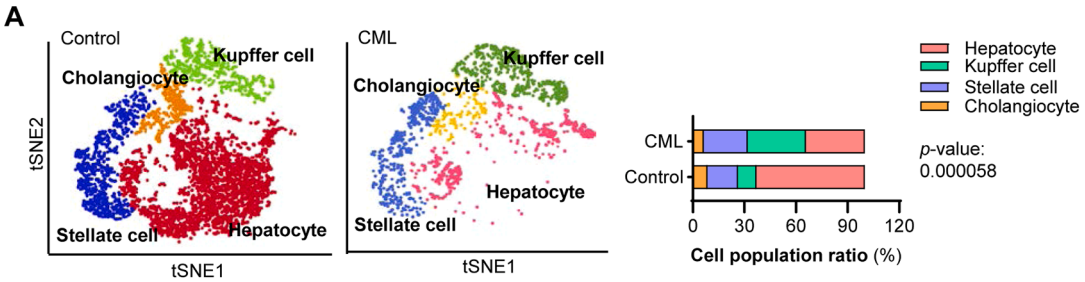

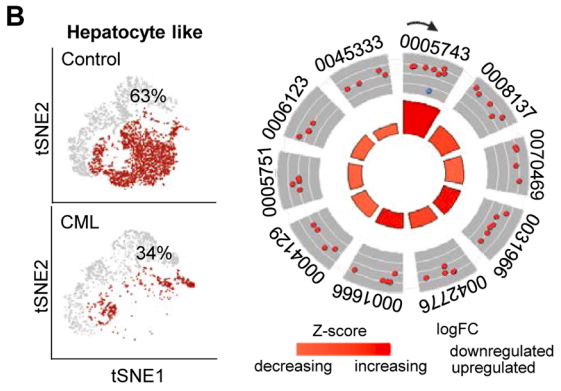

GO ID	Description
0005743	mitochondrial inner membrane
0008137	NADH dehydrogenase activity
0070469	respirasome
0031966	mitochondrial membrane
0042776	mitochondrial ATP synthesis
0001666	response to hypoxia
0004129	cytochrome-c oxidase activity
0005751	mitochondrial respiratory chain complex IV
0006123	mitochondrial electron transport
0045333	cellular respiration

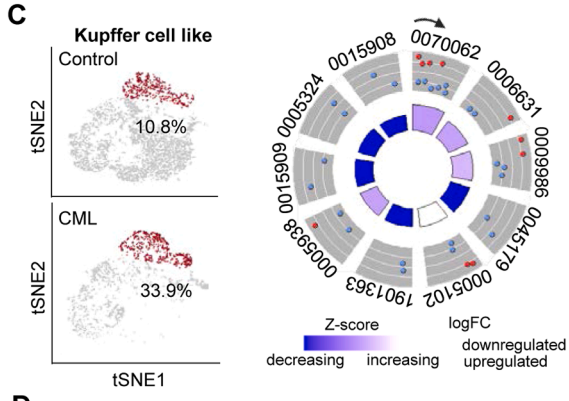

GO ID	Description
70062	extracellular exosome
6631	fatty acid metabolic process
9986	cell surface
45179	apical cortex
5102	signaling receptor binding
1901363	heterocyclic compound binding
5938	cell cortex
15909	long-chain fatty acid transport
5324	long-chain fatty acid transmembrane transporter activity
15908	fatty acid transport

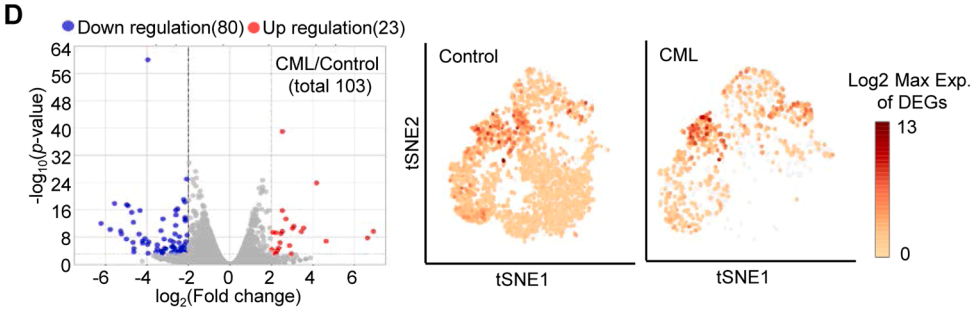

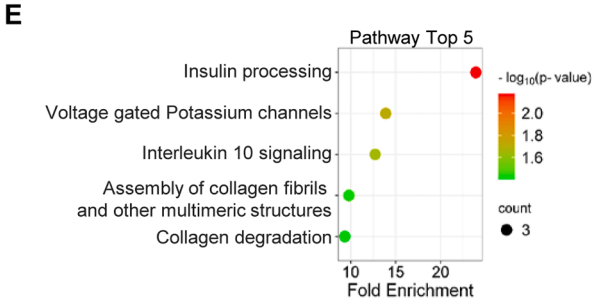

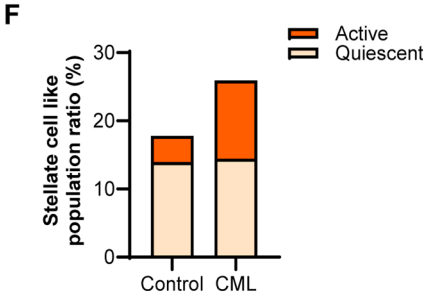

(caption on next page)

Fig. 5. Single-cell profiling of recovered cell composition and cell-type-associated programs after CML exposure. (A) t-SNE visualization of hepatocyte-like, Kupffer cell-like, stellate cell-like, and cholangiocyte-like populations in control and CML-treated HLOs, with relative proportions of recovered annotated cells shown for each condition. (B) Hepatocyte-like clusters and Gene Ontology (GO) enrichment analysis of differentially expressed genes, highlighting mitochondrial and respiration-associated transcriptional programs. (C) Kupffer cell-like clusters and GO enrichment analysis of differentially expressed genes, showing enrichment of fatty-acid metabolism, fatty-acid transport, receptor-binding, and cell-surface-associated terms. (D) Volcano plot of genes differentially expressed between CML-treated and control recovered cells (103 genes at the indicated thresholds; 80 downregulated and 23 upregulated). (E) Pathway enrichment analysis of the differentially expressed genes, showing the top enriched pathways, including collagen assembly/degradation, IL-10 signalling, insulin processing, and ion-channel-related pathways. (F) Relative distribution of inferred active- and quiescent-state stellate cell-like populations in control and CML-treated HLOs. Data are presented as means ± SEMs, and statistical significance determined using Student's *t*-test or ANOVA, where appropriate (*P < 0.05, **P < 0.01, ***P < 0.001, ****P < 0.0001). CML, Nε-carboxymethyl-lysine; FC, fold change; GO, Gene Ontology; scRNA-seq, single-cell RNA sequencing; t-SNE, t-distributed stochastic neighbour embedding.

alone; all-trans-retinoid was present during the final 24 h of the 72-h exposure period (Fig. 7C; Fig. S8C). These findings indicate that the CML-associated loss of the retinoid-storage phenotype is pharmacologically modifiable. Because inhibitor-alone groups also influenced retinoid fluorescence, however, the extent to which these effects reflect a stellate-cell-specific rescue remains unresolved.

Bay 11–7082 co-treatment significantly attenuated the CML-induced increases in mitochondrial respiration after 2 h, including basal, ATP-linked, maximal, and spare respiratory capacity (Fig. 7D). Computational analyses further identified a predicted NF-κB-associated network and enrichment of mitochondrial-related target genes in CML-treated HLOs (Fig. S8D–F). Together, these findings support a functional association between NF-κB-related signalling and CML-induced bioenergetic remodelling. Because a Bay 11–7082-alone group was not included, a direct suppressive effect of Bay 11–7082 on mitochondrial respiration cannot be excluded.

The schematic in Fig. 7E integrates the lipid-accumulation, cellular-injury, inflammatory, mitochondrial, and fibrogenic findings with the pharmacological perturbation results into a proposed working model. Collectively, the intervention studies demonstrate that multiple components of the CML-associated HLO phenotype are pharmacologically modifiable and support the involvement of oxidative stress, metabolic activity, macrophage-associated processes, and NF-κB-related signalling in the coordinated multicellular response to CML. The precise cell-specific sequence and pathway directionality remain to be established.

4. Discussion

This study identifies hepatic CML as an AGE-related feature associated with steatotic liver and shows that CML induces coordinated metabolic, inflammatory, and fibrogenic responses in multicellular HLOs. Across independent human liver datasets, AGE–RAGE pathway activity was associated with steatosis- and steatohepatitis-related features, whereas direct biospecimen measurements showed an increase in hepatic CML without a corresponding increase in total hepatic AGEs or circulating CML. This distinction between tissue and serum measurements argues against treating circulating AGE abundance as a complete surrogate for local hepatic glycation burden and provides a rationale for focusing on CML rather than AGEs as an undifferentiated class. Previous clinical studies have likewise demonstrated measurable circulating AGE and CML species but indicate that circulating concentrations represent only one component of systemic AGE exposure and may not directly reflect tissue accumulation [18,19].

The experimental model comparison further indicates that the biological response to CML is strongly influenced by cellular and tissue context. Oral CML administration caused hepatic CML accumulation and induced AGE–RAGE- and TGF-β-associated transcriptional changes in mice, but these molecular alterations did not progress to overt histological fibrosis under the tested regimen. Previous studies have similarly shown that chronic free or dietary CML exposure modifies metabolic and hepatic phenotypes under high-fat dietary conditions [9,11]. Nevertheless, mouse models of steatotic liver disease show variable correspondence with human disease at the transcriptomic level [20], emphasizing the importance of model context when extrapolating mechanistic findings.

HepG2 monolayers and spheroids likewise responded readily to OA but showed limited CML-associated lipid accumulation. Although HepG2 cells provide a reproducible hepatocyte-focused system, they incompletely reproduce differentiated human hepatic metabolism and multicellular signalling [21]. The limited phenotypes observed in the mouse and HepG2 systems therefore suggest that the magnitude and complexity of the CML response are influenced, at least in part, by cellular composition and tissue context rather than indicating biological inactivity of CML.

The HLO model was characterized before CML exposure to establish that the observed responses arose in a multicellular hepatic platform rather than being inferred solely from post-treatment clustering. Untreated HLOs showed hepatic lineage-marker expression, epithelial organization, hepatocyte- and biliary-associated proteins, albumin and apolipoprotein B secretion, and cluster-level hepatocyte-, biliary-, stellate-, and myeloid-associated transcriptional signatures. This orthogonal baseline characterization is important because treatment-associated changes in annotated cell proportions cannot by themselves establish lineage identity or selective expansion.

The HLO system should also be considered in the context of complementary human three-dimensional liver models. Primary human hepatocyte spheroids maintain differentiated hepatic functions and have been extensively characterized for liver injury and disease modelling [22], while hepatic 3D spheroids developed by Kozyra and colleagues reproduce steatosis and insulin resistance [23]. In contrast, hiPSC-derived multicellular HLOs permit hepatocyte-, immune-, and stellate-like populations to be examined within a shared three-dimensional microenvironment [24–26]. Single-cell analyses have further demonstrated that MASLD organoid responses are stimulus dependent, with distinct metabolic and profibrotic stimuli producing different inflammatory and fibrogenic states [27]. The present study leverages this multicellular context to investigate how a defined AGE species influences coordinated hepatic responses.

The concentration-response analysis directly addressed whether the HLO phenotype depended on CML exposure level. CML increased lipid accumulation from 100 μM and produced progressively stronger effects at 250 and 500 μM, while the time-course analysis showed gradual accumulation during prolonged exposure. CML and OA nevertheless separated by bulk-transcriptomic profiling despite partially overlapping lipid and structural phenotypes. This divergence is consistent with the observation that distinct metabolic and profibrotic stimuli generate different cellular and molecular states in liver organoid systems [27]. Thus, the CML response appears molecularly distinguishable from OA-driven lipotoxicity despite partially overlapping steatotic features.

The 250 μM CML condition should be interpreted as a mechanistic stress paradigm rather than as a direct clinical dose equivalent. Quantitative analyses of human plasma demonstrate CML concentrations substantially below the nominal concentrations used in many experimental systems [18], whereas clinical studies of circulating AGEs in metabolic liver disease indicate that serum measurements do not necessarily represent local hepatic exposure [19]. Moreover, protein-bound CML can accumulate in tissues independently of circulating free CML [4]. In the present study, hepatic CML was increased in steatotic human liver despite unchanged serum CML, and hepatic accumulation was also detected in CML-treated and HFD-fed mice.

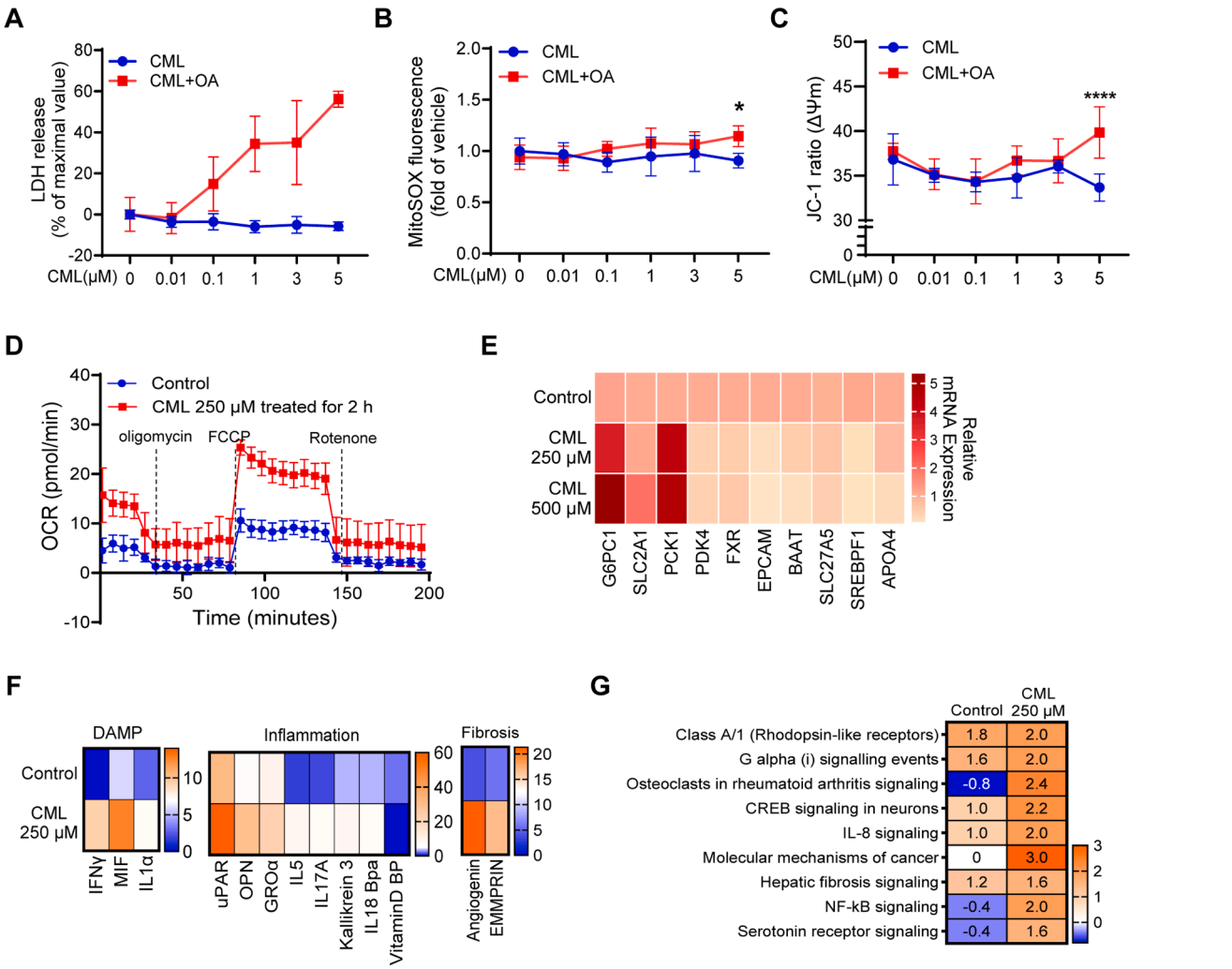

(caption on next page)

Fig. 6. Functional assessment of context-dependent hepatocyte injury and concurrent bioenergetic, inflammatory, and fibrogenic responses. (A) LDH release in primary mouse hepatocytes exposed to CML (0.01–5 μM) for 24 h in the absence or presence of oleic acid (OA; 200 μM). CML alone produced little LDH release across the tested range, whereas LDH release was greater at higher CML concentrations in the presence of OA. (B, C) Mitochondrial parameters in primary mouse hepatocytes exposed to CML with or without OA. (B) MitoSOX fluorescence showed limited changes across the tested conditions. (C) JC-1 ratio was increased at the highest CML concentration under OA co-exposure, indicating an alteration in mitochondrial membrane-potential-related signalling without evidence of depolarization. (D) Representative oxygen consumption rate (OCR) profiles of control and CML-treated HLOs following 2 h exposure to CML (250 μM), measured using Seahorse XF analysis. Quantification of mitochondrial respiration parameters is shown in Fig. S6A. (E) Relative mRNA expression of hepatic metabolic and functional genes in HLOs treated with CML. (F) Semiquantitative cytokine-array profile of DAMP-, inflammation-, and fibrosis-associated mediators in HLO culture supernatants after 3 days of CML exposure. One membrane was analysed per condition, with duplicate capture spots representing technical replicates. (G) Pathway analysis of the cytokine-array profile, including NF-κB- and hepatic-fibrosis-associated signalling categories. (H) Independent validation of inflammatory activation in CML-treated HLOs by TNF-α ELISA and IL6 qRT-PCR. (I) qRT-PCR analysis of stellate-activation-associated genes COL1A1, ACTA2, LRP1, and PDGFRB. (J) Retinoid-storage assay in control and CML-treated HLOs. HLOs were exposed to CML for 72 h, with all-trans-retinoid added during the final 24 h. Representative fluorescence and bright-field images and quantification are shown. Scale bar, 100 μm. (K) Masson's trichrome staining and quantification of collagen-positive area in control and CML-treated HLOs. Scale bar, 25 μm. Data are presented as means ± SEMs. Statistical significance was determined using Student's *t*-test or one-way/two-way ANOVA, as appropriate. $^{*}P < 0.05$, $^{**}P < 0.01$, $^{***}P < 0.001$, $^{****}P < 0.0001$. CML, Nε-carboxymethyl-lysine; OA, oleic acid; LDH, lactate dehydrogenase; OCR, oxygen consumption rate; HLO, human liver organoid; DAMP, damage-associated molecular pattern.

Table 1
Clinical characteristics of human serum donors and CAP-based liver fat quantification.

#	Serum ID	Diagnosis	Sex	Age	CAP (dB/m)
1	1027	Normal	Female	21	115
2	44	Normal	Female	59	131
3	577	Normal	Female	68	128
4	160	Normal	Female	61	107
5	235	Normal	Female	36	119
6	476	Normal	Male	78	128
7	14	Steatosis	Male	56	400
8	45	Steatosis	Female	38	397
9	167	Steatosis	Male	46	395
10	194	Steatosis	Male	27	394
11	223	Steatosis	Female	65	400
12	296	Steatosis	Female	66	387

Twelve human serum samples were obtained from normal subjects (n = 6) and patients diagnosed with steatosis (n = 6). Controlled attenuation parameter (CAP) values were measured using FibroScan and used to stratify subjects according to steatosis status based on hepatic steatosis severity. Clinical data include age, sex, and serum ID. A CAP value ≥ 280 dB/m is commonly used to indicate moderate-to-severe hepatic steatosis.

Matrix density and diffusion constraints inherent to three-dimensional organoids may additionally influence the relationship between nominal medium concentration and effective cellular exposure. The concentration-response and time-course data therefore support the internal consistency of the HLO phenotype but do not establish that an equivalent free-CML concentration occurs in human liver.

Mechanistically, the combined results support coordinated mitochondrial, inflammatory, and fibrogenic responses rather than a single linear pathway. CML increased mitochondrial respiratory demand together with proton leak, a pattern consistent with bioenergetic stress and reduced coupling efficiency rather than uniformly enhanced mitochondrial function. Importantly, previous work from our group demonstrated that CML can disrupt mitochondrial fatty-acid metabolism through regulation of carnitine palmitoyltransferase 2 in a diabetic nephropathy model [28]. Although that study was conducted in a renal disease context, it provides independent mechanistic support for an association between CML exposure and mitochondrial metabolic dysfunction. The present HLO findings extend this concept to a multicellular hepatic system without implying that the same molecular pathway necessarily operates identically across tissues.

These mitochondrial changes coincided with altered hepatic metabolic programs and the release or induction of DAMP-, cytokine-, and fibrosis-associated mediators. Single-cell analyses associated mitochondrial and metabolic transcriptional changes primarily with hepatocyte-like populations and lipid-handling programs with Kupffer-like populations. Liver-resident macrophages are heterogeneous and adopt context-dependent inflammatory and tissue-remodelling phenotypes [29]. Single-cell analyses of human liver fibrosis have also demonstrated extensive interactions among macrophage and mesenchymal populations within the fibrotic niche [30]. These observations provide a biological framework for interpreting the coordinated immune- and stellate-associated responses observed in CML-treated HLOs without establishing the direction of intercellular signalling.

Stellate-like cells exhibited an activated transcriptional state accompanied by reduced retinoid storage and increased collagen-positive area, providing phenotypic support for fibrogenic remodelling. Metabolic reprogramming is increasingly recognized as an integral component of hepatic stellate-cell activation, with simultaneous increases in glycolysis and oxidative phosphorylation reported during

Table 2
Clinical and histological characteristics of human liver tissue samples.

Sample #	1	2	3	4	5	6
Sample ID	1–35	1–38	1–40	1–61	1–68	1–81
Diagnosis	Normal	Normal	Normal	Steatosis	Steatosis	Steatosis
Sex	Female	Female	Male	Female	Male	Female
Age	55	56	39	51	27	66
NAS	0	0	0	6	6	6
Steatosis	0	0	0	3	3	3
Inflammation	0	0	0	2	2	1
Ballooning	0	0	0	1	1	2
ALT (U/L)	34	5	14	21	31	47
AST (U/L)	21	11	18	13	18	21
GGT (U/L)	26	8	20	34	25	27

Liver tissues were classified as histologically normal or steatotic. Histological features were assessed using the NAFLD Activity Score (NAS), which comprises steatosis, lobular inflammation, and hepatocellular ballooning scores, with a total score ranging from 0 to 8. An NAS ≥ 5 is generally indicative of probable steatohepatitis, previously termed nonalcoholic steatohepatitis (NASH) and now reclassified as metabolic dysfunction-associated steatohepatitis (MASH). Serum liver enzyme levels (alanine aminotransferase [ALT], aspartate aminotransferase [AST], and gamma-glutamyl transferase [GGT]) are presented as markers of hepatic injury. All data are based on histologically verified liver tissues provided by a collaborating clinical institution.

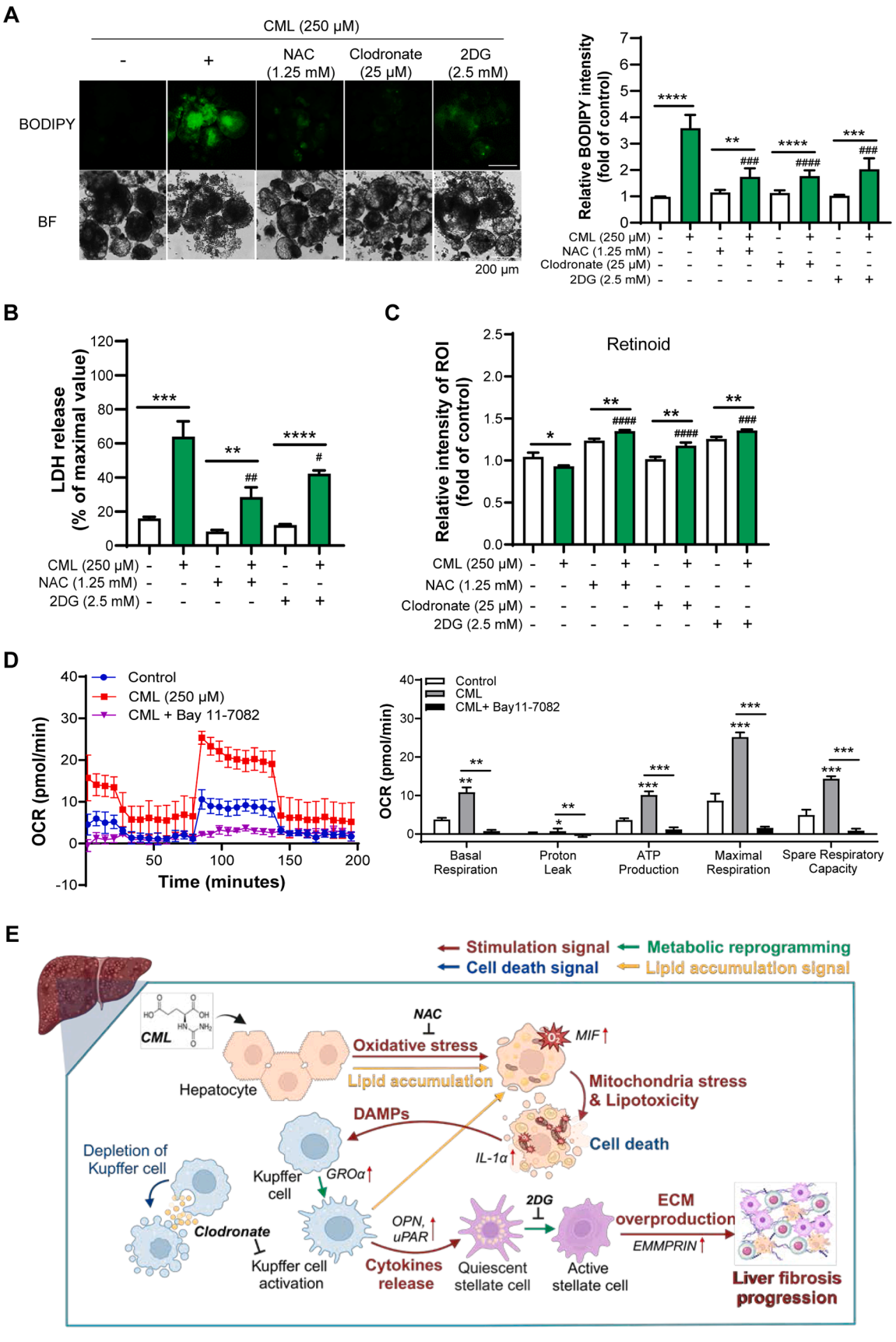

(caption on next page)

Fig. 7. Pharmacological modulation of selected CML-associated HLO phenotypes. (A) BODIPY staining of lipid droplets in HLOs treated with CML (250 μM) alone or in combination with inhibitors: NAC (1.25 mM, antioxidant), clodronate (25 μM, macrophage depletion agent), and 2DG (2.5 mM, stellate cell metabolic inhibitor). Bright-field (BF) images are shown below the fluorescent images. Scale bar: 200 μm. Quantification of BODIPY fluorescence intensity is shown as fold change relative to control. $^{**}P < 0.01$, $^{***}P < 0.001$, $^{****}P < 0.0001$ vs. control; $^{\#\#\#}P < 0.001$, $^{\#\#\#\#}P < 0.0001$ vs. CML. (B) LDH release after 72-h treatment with CML alone or in combination with the indicated compounds. $^{**}P < 0.01$, $^{***}P < 0.001$, $^{****}P < 0.0001$ vs. control; $^{\#}P < 0.05$, $^{\#\#}P < 0.01$ vs. CML. (C) Retinoid-storage assay following CML treatment with or without the indicated compounds. All-trans-retinoid was present during the final 24 h of the 72-h exposure period. $^{*}P < 0.05$, $^{**}P < 0.01$ vs. control; $^{\#\#\#}P < 0.001$, $^{\#\#\#\#}P < 0.0001$ vs. CML. (D) OCR was measured using Seahorse XF analysis after 2-h treatment with CML (250 μM), with or without NF-κB inhibitor (Bay 11–7082, 10 μM). Left: real-time OCR profile. Right: Quantification of mitochondrial respiration parameters. (E) Proposed working model integrating the lipid, bioenergetic, inflammatory, and fibrogenic responses observed after CML exposure and their pharmacological modulation. The depicted intercellular relationships represent candidate mechanistic links and do not establish cell-specific sequence or causal directionality. 2DG, 2-deoxy-D-glucose; BODIPY, 4,4-difluoro-1,3,5,7,8-pentamethyl-4-bora-3a,4a-diaza-s-indacene; CML, Nε-carboxymethyl-lysine; HLO, human liver organoid; LDH, lactate dehydrogenase; NAC, N-acetylcysteine.

stellate-cell activation [31]. CML-specific stellate-cell studies have likewise demonstrated oxidative stress, collagen production, and fibrogenic responses after CML exposure [14,15]. More broadly, AGEs promote hepatic stellate-cell proliferation and activation, stimulate NADPH oxidase-dependent reactive oxygen species generation, and exacerbate experimental hepatic fibrosis [13,16,17]. Taken together, these findings support concurrent metabolic, inflammatory, and stellate-cell responses but do not establish which cell type initiates the process or the directionality of intercellular signalling.

The anti-RAGE experiment further supports a contribution of RAGE-associated signalling to the CML-induced lipid-accumulation phenotype, as RAGE blockade reduced BODIPY accumulation. This finding is consistent with the ability of CML-containing protein adducts to engage RAGE and activate downstream signalling pathways [6] and with previous evidence implicating CML–RAGE signalling in hepatic inflammation and fatty liver progression [7,10]. However, the experimental free-CML stimulus used here should not be assumed to behave identically to protein-bound CML ligands. The greater response to CML than to CEL, MG-H1, or MGO further suggests that the observed phenotype is not a uniform response to all AGE-related compounds, but it does not establish a uniquely CML-specific receptor mechanism. Differences in receptor affinity, cellular uptake, chemical stability, protein modification, and signalling kinetics remain plausible and require direct comparative evaluation.

Pharmacological perturbation experiments identified several signalling and metabolic nodes associated with the HLO response. NAC attenuated selected lipid and injury-related outcomes, consistent with its antioxidant properties and with previous evidence for protective effects in metabolic liver injury [32,33]. 2DG attenuated selected phenotypes, supporting a contribution of glucose-dependent metabolic activity, although its broad effects on cellular energy metabolism preclude assignment of a specific glycolytic mechanism. Clodronate also attenuated selected responses, supporting a contribution of macrophage-associated activity. Classical studies have demonstrated that liposome-delivered clodronate can deplete Kupffer cells [34]; however, the present organoid experiment should not be interpreted as demonstrating selective Kupffer-cell depletion unless equivalent delivery and depletion were directly verified.

Bay 11–7082 co-treatment attenuated CML-induced increases in mitochondrial respiration, supporting an association between NF-κB-related signalling and CML-induced bioenergetic changes. Although Bay 11–7082 has historically been used as an inhibitor of NF-κB-associated signalling, it can also affect components of the ubiquitin system and other inflammatory signalling pathways [35]. The present findings are therefore interpreted as pharmacological support for involvement of NF-κB-related signalling rather than pathway-specific causal proof.

Taken together, the pharmacological experiments provide mechanistic support but do not establish a definitive linear pathway or cell-specific causality. NAC and 2DG exert broad metabolic effects, clodronate is not inherently a selective readout of Kupffer-like signalling in the present organoid context, and the absence of a Bay 11–7082-alone group prevents exclusion of a direct suppressive effect on mitochondrial respiration. These limitations support interpreting the perturbation studies as complementary mechanistic evidence rather than definitive pathway mapping.

Patient-derived serum cytokine and liver proteomic profiles showed inflammatory and remodelling themes that partially overlapped with those observed in CML-treated HLOs, including tissue-level IL-6–JAK–STAT3 pathway enrichment. This cross-system concordance supports the disease relevance of the organoid-associated response but does not establish CML as the sole upstream cause of the patient-associated signatures. The serum cytokine array was a semi-quantitative screen based on technical duplicate spots from one representative specimen per group, and the patient cohorts were small. These findings are therefore best interpreted as convergent translational support that requires validation in larger, clinically stratified cohorts with direct measurement of hepatic CML burden.

Several limitations define the boundaries of the present conclusions. First, HLOs lack vascular perfusion and do not fully reproduce the endocrine, endothelial, and adaptive immune environment of the liver, limitations common to current liver organoid platforms [25]. Second, fewer viable cells were recovered from CML-treated than control HLOs for scRNA-seq; differences in annotated cell-type proportions may therefore reflect, at least in part, differential survival or dissociation/recovery bias and should not be interpreted as direct evidence of selective proliferation or depletion. Third, the temporal sequence and directionality of signalling among hepatocyte-, Kupffer-, and stellate-like populations were not resolved. Fourth, the organoid exposure concentrations are mechanistically informative but should not be interpreted as clinical dose equivalents. Finally, the limited patient sample sizes and semiquantitative array design restrict causal and biomarker inference.

Future studies incorporating time-resolved single-cell profiling, cell-type-specific perturbation, conditioned-medium experiments, vascularized or more immunologically complex HLO models, and larger patient cohorts spanning fibrosis stages will be important for defining the temporal sequence, cell-type-specific mechanisms, and clinical significance of hepatic CML-associated responses.

Overall, these findings support hepatic CML as a biologically relevant AGE-related feature of steatotic liver disease and demonstrate that multicellular HLOs can capture coordinated mitochondrial, inflammatory, and fibrogenic responses that are only partially represented in simpler experimental systems. The study therefore provides a mechanistically informative human multicellular framework for investigating CML-associated liver injury while also defining the experimental and translational limits of the current model.

5. Conclusion

This study identifies hepatic CML as an AGE-related feature associated with steatotic liver and demonstrates coordinated metabolic, mitochondrial, inflammatory, and fibrogenic responses to CML in multicellular HLOs. These responses were only partially reproduced in mouse and HepG2 models, underscoring the importance of tissue context. Patient-derived serum and liver profiles showed partial concordance with CML-associated HLO signatures, supporting the

translational relevance of the model. The CML–HLO system therefore provides a useful human multicellular platform for investigating AGE-associated liver pathology, although the initiating cell type, signalling directionality, and clinical exposure equivalence remain to be established.

CRediT authorship contribution statement

Jin Young Min: Writing – review & editing, Writing – original draft, Visualization, Validation, Methodology, Investigation, Formal analysis, Data curation. **Min Ji Gu:** Writing – review & editing, Writing – original draft, Methodology, Investigation, Formal analysis, Data curation. **Hye Min Kim:** Writing – review & editing, Visualization, Validation, Methodology, Investigation, Formal analysis. **Donghwan Kim:** Writing – review & editing, Investigation, Data curation. **Geul Bang:** Writing – review & editing, Investigation, Data curation. **Sang-Yeop Lee:** Writing – review & editing, Investigation, Data curation. **Hae Won Jung:** Writing – review & editing, Investigation, Data curation. **Kwan Soo Hong:** Writing – review & editing, Writing – original draft, Investigation. **Dae Won Jun:** Writing – review & editing, Supervision, Resources, Investigation. **Seung Min Lee:** Writing – review & editing, Investigation, Formal analysis. **Sang Keun Ha:** Writing – review & editing, Writing – original draft, Supervision, Methodology, Funding acquisition, Conceptualization. **Eun Hee Han:** Writing – review & editing, Writing – original draft, Supervision, Project administration, Methodology, Funding acquisition, Conceptualization.

Author contributions: CRediT

J.Y.M., M.J.G., and H.M.K. contributed equally to this work. J.Y.M., M.J.G., H.M.K., D.H.K., G.B., S.M.L., and H.W.J. performed the experiments and collected the data. G.B., J.Y.M., and S.Y.L. performed the proteomic and single-cell RNA sequencing (scRNA-seq) analyses and associated bioinformatics processing. K.S.H., D.W.J., S.K.H., and E.H.H. contributed to data analysis, interpretation, and overall study design. J.Y.M., M.J.G., and E.H.H. wrote the original draft of the manuscript, with additional contributions and critical revisions from J.Y.M. and H.M.K. S.K.H. and E.H.H. supervised the project and provided critical guidance throughout the study. All authors contributed to the review and editing of the manuscript and approved the final version.

Ethics declaration

Written informed consent to take part in the study and to publish the article has been obtained from all participants or their legal representatives. The privacy rights of participants have been observed.

This study included organ or tissue donors. This study includes human biological material and consent was obtained by donors, or their next of kin or legal representatives, for use in this study and for publication of the article. The samples used in this research were not sourced from executed prisoners or prisoners of conscience.

This study was performed in compliance with relevant laws, regulatory frameworks and guidelines where the research took place. This study was conducted in accordance with Declaration of Helsinki and applicable Korean regulations and institutional guidelines. This study was approved by the Institutional Review Board of Hanyang University Hospital. (Approval No. HYUH 2019–12–028–022)

This study was conducted in accordance with the ARRIVE (Animal Research: Reporting of In Vivo Experiments) guidelines. This study was approved by the Korea Food Research Institute Institutional Animal Care and Use Committee. (Approval No. KFRI-M-21057)

Compliance with Ethics Requirements

All animal experiments were approved by the Korea Food Research Institute Institutional Animal Care and Use Committee (protocol no. KFRI-M-21057) and conducted in accordance with its guidelines. This study adhered to the ARRIVE guidelines for reporting animal research.

Human serum and liver tissue samples were obtained with approval from the Institutional Review Board of Hanyang University Hospital (IRB no. HYUH 2019–12–028–022) and used in accordance with the Declaration of Helsinki and applicable institutional ethical guidelines. Written informed consent was obtained from all participants.

Declaration of Generative AI and AI-assisted technologies in the writing process

During the preparation of this work, the authors used ChatGPT (OpenAI) for language editing and improving the clarity and organization of the manuscript. The authors reviewed and edited the output as needed and take full responsibility for the content of the published article.

Funding

This work was supported by the National Research Foundation of Korea (NRF) grant funded by the Korean government (MSIT) (NRF-2020R1C1C1012542 to E.H.H.); grants from the Korea Basic Science Institute (C623100, C612110, C612594, C623500, and S610000 to E.H.H.; C623200 to G.B.); a grant from the Korea Food Research Institute (E0210203 to S.K.H.); and a Korea Evaluation Institute of Industrial Technology (KEIT) grant funded by the Korean government (MOTIE) (RS-2025–25462597 to K.S.H.).

Declaration of competing Interest

The authors declare that they have no known competing financial interests or personal relationships that could have appeared to influence the work reported in this paper.

Acknowledgements

We acknowledge the use of facilities and equipment (IDs: AB21, AS45, BIO37) at the Korea Basic Science Institute (Cheongju, Republic of Korea). We also thank Editage (www.editage.com) for English language editing and BioRender (www.biorender.com) for assistance with figure illustrations.

Appendix A. Supporting information

Supplementary data associated with this article can be found in the online version at doi:10.1016/j.phrs.2026.109653.

Data availability

The data that has been used is confidential.

References

[1] R. Loomba, S.L. Friedman, G.I. Shulman, Mechanisms and disease consequences of nonalcoholic fatty liver disease, Cell 184 (2021) 2537–2564, https://doi.org/10.1016/j.cell.2021.04.015.
[2] A. Rojas, C. Lindner, I. Schneider, I. Gonzalez, J. Uribarri, The RAGE axis: A relevant inflammatory hub in human diseases, Biomolecules 14 (2024) 412, https://doi.org/10.3390/biom14040412.
[3] S. Reddy, J. Bichler, K.J. Wells-Knecht, S.R. Thorpe, J.W.N. Baynes, ε-(Carboxymethyl)lysine is a dominant advanced glycation end product (AGE) antigen in tissue proteins, Biochemistry 34 (1995) 10872–10878, https://doi.org/10.1021/bi00034a021.
[4] M. Li, M. Zeng, Z. He, Z. Zheng, F. Qin, G. Tao, et al., Increased accumulation of protein-bound Nε-(carboxymethyl)lysine in tissues of healthy rats, J. Agric. Food Chem. 63 (2015) 1658–1663, https://doi.org/10.1021/jf505063t.
[5] M.X. Fu, J.R. Requena, A.J. Jenkins, T.J. Lyons, J.W. Baynes, S.R. Thorpe, The advanced glycation end product, Nε-(carboxymethyl)lysine, is a product of both lipid peroxidation and glycoxidation reactions, J. Biol. Chem. 271 (1996) 9982–9986, https://doi.org/10.1074/jbc.271.17.9982.

[6] T. Kislinger, C. Fu, B. Huber, W. Qu, A. Taguchi, S.D. Yan, et al., Nε-(Carboxymethyl)lysine adducts of proteins are ligands for receptor for advanced glycation end products that activate cell signaling pathways and modulate gene expression, J. Biol. Chem. 274 (1999) 31740–31749, https://doi.org/10.1074/jbc.274.44.31740.
[7] K.H.J. Gaens, P.M.G. Niessen, S.S. Rensen, W.A. Buurman, J.W.M. Greve, A. Driessen, et al., Endogenous formation of Nε-(carboxymethyl)lysine is increased in fatty livers and induces inflammatory markers in an in vitro model of hepatic steatosis, J. Hepatol. 56 (2012) 647–655, https://doi.org/10.1016/j.jhep.2011.07.028.
[8] E. Yagmur, F. Tacke, C. Weiss, B. Lahme, M.P. Manns, P. Kiefer, et al., Elevation of Nε-(carboxymethyl)lysine-modified advanced glycation end products in chronic liver disease is an indicator of liver cirrhosis, Clin. Biochem. 39 (2006) 39–45, https://doi.org/10.1016/j.clinbiochem.2005.07.016.
[9] M. Li, M. Zeng, Z. He, Z. Zheng, F. Qin, G. Tao, et al., Effects of long-term exposure to free Nε-(carboxymethyl)lysine on rats fed a high-fat diet, J. Agric. Food Chem. 63 (2015) 10995–11001, https://doi.org/10.1021/acs.jafc.5b05750.
[10] Q. Pang, Z. Sun, C. Shao, H. Cai, Z. Bao, L. Wang, et al., CML/RAGE signal bridges a common pathogenesis between atherosclerosis and non-alcoholic fatty liver, Front. Med. (Lausanne) 7 (2020) 583943, https://doi.org/10.3389/fmed.2020.583943.
[11] H.B. Lee, J.H. Choi, D. Kim, K.W. Lee, S.K. Ha, S.H. Lee, et al., Dietary Nε-(carboxymethyl)lysine is a trigger of non-alcoholic fatty liver disease under high-fat consumption, Food Chem. Toxicol. 180 (2023) 114010, https://doi.org/10.1016/j.fct.2023.114010.
[12] R. Patel, S.S. Baker, W. Liu, S. Desai, R. Alkhouri, R. Kozielski, et al., Effect of dietary advanced glycation end products on mouse liver, PLoS. One 7 (2012) e35143, https://doi.org/10.1371/journal.pone.0035143.
[13] M. Goodwin, C.B. Herath, Z. Jia, C. Leung, M.T. Coughlan, J.M. Forbes, et al., Advanced glycation end products augment experimental hepatic fibrosis, J. Gastroenterol. Hepatol. 28 (2013) 369–376, https://doi.org/10.1111/jgh.12042.
[14] W.H. Hsu, B.H. Lee, Y.W. Hsu, T.M. Pan, Peroxisome proliferator-activated receptor-γ activators monascin and rosiglitazone attenuate carboxymethyllysine-induced fibrosis in hepatic stellate cells through regulating the oxidative stress pathway but independent of receptor for advanced glycation end products signaling, J. Agric. Food Chem. 61 (2013) 6873–6879, https://doi.org/10.1021/jf402082g.
[15] B.H. Lee, W.H. Hsu, Y.W. Hsu, T.M. Pan, Suppression of dimerumic acid on hepatic fibrosis caused from carboxymethyl-lysine by attenuating oxidative stress depends on Nrf2 activation in hepatic stellate cells, Food Chem. Toxicol. 62 (2013) 413–419, https://doi.org/10.1016/j.fct.2013.09.007.
[16] K. Iwamoto, K. Kanno, H. Hyogo, S.I. Yamagishi, M. Takeuchi, S. Tazuma, et al., Advanced glycation end products enhance the proliferation and activation of hepatic stellate cells, J. Gastroenterol. 43 (2008) 298–304, https://doi.org/10.1007/s00535-007-2152-7.
[17] E.L.M. Guimarães, C. Empsen, A. Geerts, L.A. Van Grunsven, Advanced glycation end products induce production of reactive oxygen species via the activation of NADPH oxidase in murine hepatic stellate cells, J. Hepatol. 52 (2010) 389–397, https://doi.org/10.1016/j.jhep.2009.12.007.
[18] D. Wang, J. Wang, X. Liu, K. Du, H. Liu, X. Yang, et al., Quantifying carboxymethyl lysine and carboxyethyl lysine in human plasma, BMC Biotechnol. 24 (2024) 12, https://doi.org/10.1186/s12896-024-00838-5.
[19] S.A. Palma-Duran, M.D. Kontogianni, A. Vlassopoulos, S. Zhao, A. Margariti, M. Georgoulis, et al., Serum levels of advanced glycation end-products and the decoy soluble receptor for AGEs can identify non-alcoholic fatty liver disease in age-, sex-, and BMI-matched normoglycemic adults, Metabolism 83 (2018) 120–127, https://doi.org/10.1016/j.metabol.2018.01.016.
[20] A. Teufel, T. Itzel, W. Erhart, M. Brosch, X.Y. Wang, Y.O. Kim, et al., Comparison of gene expression patterns between mouse models of nonalcoholic fatty liver disease and liver tissues from patients, e10, Gastroenterology 151 (2016) 513–525, https://doi.org/10.1053/j.gastro.2016.05.051.
[21] L.A. Stanley, C.R. Wolf, Through a glass, darkly? HepaRG and HepG2 cells as models of human phase I drug metabolism, Drug. Metab. Rev. 54 (2022) 46–62, https://doi.org/10.1080/03602532.2022.2039688.
[22] C.C. Bell, D.F.G. Hendriks, S.M.L. Moro, E. Ellis, J. Walsh, A. Renblom, et al., Characterization of primary human hepatocyte spheroids as a model system for drug-induced liver injury, liver function and disease, Sci. Rep. 6 (2016) 25187, https://doi.org/10.1038/srep25187.
[23] M. Kozyra, I. Johansson, Å. Nordling, S. Ullah, V.M. Lauschke, M. Ingelman-Sundberg, Human hepatic 3D spheroids as a model for steatosis and insulin resistance, Sci. Rep. 8 (2018) 14297, https://doi.org/10.1038/s41598-018-32722-6.
[24] R. Ouchi, S. Togo, M. Kimura, T. Shinozawa, M. Koido, H. Koike, et al., Modeling steatohepatitis in humans with pluripotent stem cell-derived organoids, Cell. Metab. 30 (2019) 374–384.e6, https://doi.org/10.1016/j.cmet.2019.05.007.
[25] S.P. Harrison, S.F. Baumgarten, R. Verma, O. Lunov, A. Dejneka, G.J. Sullivan, Liver organoids: Recent developments, limitations and potential, Front. Med. (Lausanne) 8 (2021) 574047, https://doi.org/10.3389/fmed.2021.574047.
[26] J. Bronsard, C. Savary, J. Massart, R. Viel, L. Moutaux, D. Catheline, et al., 3D multi-cell-type liver organoids: A new model of non-alcoholic fatty liver disease for drug safety assessments, Toxicol. Vitr. 94 (2024) 105728, https://doi.org/10.1016/j.tiv.2023.105728.
[27] A. Hess, S.D. Gentile, A. Ben Saad, R.U. Rahman, T. Habboub, D.S. Pratt, et al., Single-cell transcriptomics stratifies organoid models of metabolic dysfunction-associated steatotic liver disease, EMBO J. 42 (2023) e113898, https://doi.org/10.15252/embj.2023113898.
[28] J. Lee, J.Y. Hyon, J.Y. Min, Y.H. Huh, H.J. Kim, H. Lee, et al., Mitochondrial carnitine palmitoyltransferase 2 is involved in Nε-(carboxymethyl)lysine-mediated diabetic nephropathy, Pharmacol. Res. 152 (2020) 104600, https://doi.org/10.1016/j.phrs.2019.104600.
[29] C. Blériot, F. Ginhoux, Understanding the heterogeneity of resident liver macrophages, Front. Immunol. 10 (2019) 2694, https://doi.org/10.3389/fimmu.2019.02694.
[30] P. Ramachandran, R. Dobie, J.R. Wilson-Kanamori, E.F. Dora, B.E.P. Henderson, N. T. Luu, et al., Resolving the fibrotic niche of human liver cirrhosis at single-cell level, Nature 575 (2019) 512–518, https://doi.org/10.1038/s41586-019-1631-3.
[31] N. Smith-Cortinez, K. van Eunen, J. Heegsma, S.A. Serna-Salas, S. Sydor, L. P. Bechmann, et al., Simultaneous induction of glycolysis and oxidative phosphorylation during activation of hepatic stellate cells reveals novel mitochondrial targets to treat liver fibrosis, Cells 9 (2020) 2456, https://doi.org/10.3390/cells9112456.
[32] Q. Ding, R. Guo, L. Pei, S. Lai, J. Li, Y. Yin, et al., N-acetylcysteine alleviates high fat diet-induced hepatic steatosis and liver injury via regulating the intestinal microecology in mice, Food Funct. 13 (2022) 3368–3380, https://doi.org/10.1039/D1FO03952K.
[33] M. Galicia-Moreno, H.C. Monroy-Ramirez, F. Caloca-Camarena, S. Arceo-Orozco, P. Muriel, A. Sandoval-Rodriguez, et al., A new opportunity for N-acetylcysteine: An outline of its classic antioxidant effects and its pharmacological potential as an epigenetic modulator in liver diseases treatment, Naunyn Schmiede Arch. Pharmacol. 398 (2025) 2365–2386, https://doi.org/10.1007/s00210-024-03539-0.
[34] N. Van Rooijen, Sanders A. Kupffer cell depletion by liposome-delivered drugs: Comparative activity of intracellular clodronate, propamidine, and ethylenediaminetetraacetic acid, Hepatology 23 (1996) 1239–1243, https://doi.org/10.1053/jhep.1996.v23.pm0008621159.
[35] S. Strickson, D.G. Campbell, C.H. Emmerich, A. Knebel, L. Plater, M.S. Ritorto, et al., The anti-inflammatory drug BAY 11-7082 suppresses the MyD88-dependent signalling network by targeting the ubiquitin system, Biochem. J. 451 (2013) 427–437, https://doi.org/10.1042/BJ20121651.